

The CARMENES search for exoplanets around M dwarfs

Two terrestrial planets orbiting G 264–012 and one terrestrial planet orbiting GI 393*

P. J. Amado¹, F. F. Bauer¹, C. Rodríguez López¹, E. Rodríguez¹, C. Cardona Guillén^{2,3}, M. Perger^{6,7}, J. A. Caballero⁴, M. J. López-González¹, I. Muñoz Rodríguez⁵, F. J. Pozuelos^{8,25}, A. Sánchez-Rivero¹, M. Schlecker⁹, A. Quirrenbach¹⁰, I. Ribas^{6,7}, A. Reiners¹¹, J. Almenara¹², N. Astudillo-Defru¹³, M. Azzaro¹⁴, V. J. S. Béjar^{2,3}, R. Bohemann¹¹, X. Bonfils¹², F. Bouchy¹⁵, C. Cifuentes⁴, M. Cortés-Contreras⁴, X. Delfosse¹², S. Dreizler¹¹, T. Forveille¹², A. P. Hatzes¹⁶, Th. Henning⁹, S. V. Jeffers²⁴, A. Kaminski¹⁰, M. Kürster⁹, M. Lafarga^{6,7}, N. Lodieu^{2,3}, C. Lovis¹⁵, M. Mayor¹⁵, D. Montes¹⁷, J. C. Morales^{6,7}, N. Morales¹, F. Murgas^{2,3}, J. L. Ortiz¹, F. Pepe¹⁵, V. Perdelwitz^{18,21}, D. Pollaco¹⁹, N. C. Santos^{20,22}, P. Schöfer¹¹, A. Schweitzer²¹, N. C. Ségransan¹⁵, Y. Shan¹¹, S. Stock¹⁰, L. Tal-Or^{18,11}, S. Udry¹⁵, M. R. Zapatero Osorio²³, and M. Zechmeister¹¹

(Affiliations can be found after the references)

Received dd February 2021 / Accepted dd Month 2021

ABSTRACT

We report the discovery of two planetary systems, namely G 264–012, an M4.0 dwarf with two terrestrial planets ($M_b \sin i = 2.50_{-0.30}^{+0.29} M_\oplus$ and $M_c \sin i = 3.75_{-0.47}^{+0.48} M_\oplus$), and GI 393, a bright M2.0 dwarf with one terrestrial planet ($M_b \sin i = 1.71 \pm 0.24 M_\oplus$). Although both stars were proposed to belong to young stellar kinematic groups, we estimate their ages to be older than about 700 Ma. The two planets around G 264–012 were discovered using only radial-velocity (RV) data from the CARMENES exoplanet survey, with estimated orbital periods of 2.30 d and 8.05 d, respectively. Photometric monitoring and analysis of activity indicators reveal a third signal present in the RV measurements, at about 100 d, caused by stellar rotation. The planet GI 393 b was discovered in the RV data from the HARPS, CARMENES, and HIRES instruments. Its identification was only possible after modelling, with a Gaussian process (GP), the variability produced by the magnetic activity of the star. For the earliest observations, this variability produced a forest of peaks in the periodogram of the RVs at around the 34 d rotation period determined from *Kepler* data, which disappeared in the latest epochs. After correcting for them with this GP model, a significant signal showed at a period of 7.03 d. No significant signals in any of our spectral activity indicators or contemporaneous photometry were found at any of the planetary periods. Given the orbital and stellar properties, the equilibrium temperatures of the three planets are all higher than that for Earth. Current planet formation theories suggest that these two systems represent a common type of architecture. This is consistent with formation following the core accretion paradigm.

Key words. planetary systems – techniques: photometric – techniques: radial velocities – stars: individual: G 264–012, GI 393 – stars: late-type

1. Introduction

Our current understanding on the formation of low-mass planets in close-in orbits around low-mass stars is that they are abundant to at least one per star. This understanding mainly comes from statistical population analyses of the results provided by ground-based Doppler surveys (Bonfils et al. 2013; Tuomi et al. 2014) and NASA’s *Kepler* mission. *Kepler* results suggest a planet occurrence of $0.56_{-0.05}^{+0.06}$ Earth-sized planets ($1.0\text{--}1.5 R_\oplus$) per M dwarf for periods shorter than 50 d, going up to 2.5 ± 0.2 planet per star with radii $1\text{--}4 R_\oplus$ and periods shorter than 200 d (Dressing & Charbonneau 2015). More recent results, focussing on mid-M dwarfs, determine occurrences of 0.86, 1.36, and 3.07 planets with periods between 0.5 and 10 d per M3, M4, and M5 dwarf stars, respectively (Hardegree-Ullman et al. 2019).

However, despite the large number of these types of planets having been discovered by *Kepler* (in both its flavours, the original mission and the K2 extension) and the Doppler surveys, very few have bulk density determinations. This is the case because a density calculation requires both the radius and mass to be known. Radii can be measured for transiting planets, but only the brightest targets can be followed up on with a Doppler in-

strument for a mass measurement. On the other hand, Doppler discoveries have low transit probabilities (e.g. 1.5% in the case of Proxima b; Anglada-Escudé+16), making their radii difficult to obtain.

The small number of planets with precise bulk density measurements consist of transiting planets that have mass estimates to a precision better than 20% (from radial velocity or transit timing variations). From this sample, we learned that planets with masses below $5\text{--}6 M_\oplus$ appear to be rocky with interiors of terrestrial composition (Zeng et al. 2016; López-Morales et al. 2016), though they show a large range of possible internal compositions in the $3\text{--}5 M_\oplus$ range.

To be able to understand the influence of different protoplanetary disc conditions in the formation and evolution of planetary systems or the mechanisms of formation of planetary systems challenging current formation theories, such as the Jupiter-like planet GJ 3512 b around a low mass M dwarf (Morales et al. 2019), we aim to clarify the differences in the number and type of exoplanets orbiting M dwarfs and their preference to form multi-planetary systems. To move forward, we need robust statistics for planet occurrence, system architecture, and bulk density, which, in turn, means having a larger number of small

planets ($M \lesssim 3 M_{\oplus}$) with accurate mass and radius measurements. Current Doppler instruments achieve a precision close to or below 1 m s^{-1} (Mayor et al. 2003, e.g. HARPS; MAROON-X, Trifonov et al. 2021, on Gl 486; ESPRESSO, Suárez Mascareño et al. 2020, on Proxima Centauri), which is sufficient for detecting these planets orbiting M dwarfs.

We can improve our statistics by either observing bright M dwarfs to detect transiting planets and follow them up with RVs or the other way around, that is, detecting the planets in blind large RV surveys and next looking for transits. The first approach is followed, for instance, by the *Transiting Exoplanet Survey Satellite* (TESS, Ricker et al. 2015) mission, a space telescope that was built to find small planets transiting small, bright stars that could be followed up on with RV instruments such as HARPS (Mayor et al. 2003) or CARMENES (Quirrenbach et al. 2018; Bluhm et al. 2020). The second approach is followed by surveys such as CARMENES with the homonymous instrument or RedDots¹ (Jeffers et al. 2020) with HARPS, which are optimised to detect planets around our closest M dwarf neighbours with Doppler measurements, looking for transits next.

In this work, we report the results of a long-term spectroscopic and photometric monitoring campaign of G 264–012 and Gl 393, an M4.0V and an M2.0V dwarf star, respectively. The combined analysis of G 264–012 confirms the presence of two super-Earths with minimum masses of about $2.5 M_{\oplus}$ and $3.8 M_{\oplus}$ with orbital periods of 2.3 d and 8.1 d, respectively. Around Gl 393, we detect a super-Earth-type planet with a minimum mass of $1.7 M_{\oplus}$ and a period of 7.0 d.

The work is organised as follows: Sect. 2 introduces the main characteristic of the stars; Sect. 3 describes the data sets, the data reduction, and the main characteristics of the instruments used in this study; Sect. 4 presents the analysis and the search for periodic signals; Sect. 5 describes the main characteristics of the planetary system and discusses them; and Sect. 6 summarises the main results.

2. The stars

G 264–012 and Gl 393 are two of the approximately 350 M dwarfs monitored during the CARMENES guaranteed time observation programme (Quirrenbach et al. 2014; Reiners et al. 2018). Table 1 provides a summary of the basic parameters of the two new exoplanet-host stars with the corresponding references.

G 264–012 (Karmn J21466+668) is a nearby, relatively bright M4.0 V star ($d \sim 16 \text{ pc}$, $J \sim 8.8 \text{ mag}$). It was the subject of investigations on astrometry (Giclas et al. 1971; Luyten 1979; Lépine & Shara 2005; Dittmann et al. 2014; Schneider et al. 2016), low-resolution spectroscopy (Lépine et al. 2013; Gaidos et al. 2014; Alonso-Floriano et al. 2015), high-resolution spectroscopy (Jeffers et al. 2018; Rajpurohit et al. 2018; Passegger et al. 2018, 2019), photometric variability (Newton et al. 2016), and speckle imaging (Janson et al. 2014). G 264–012 was repeatedly catalogued as a potential candidate for exoplanet surveys (Lépine & Gaidos 2011; Frith et al. 2013; Lépine et al. 2013; Alonso-Floriano et al. 2015; Reiners et al. 2018).

Gl 393 (Karmn J10289+008, BD+01 2447) is a closer and brighter M2.0 V star ($d \sim 7.0 \text{ pc}$, $J \sim 6.2 \text{ mag}$) that was already catalogued in the *Bonner Durchmusterung des nördlichen Himmels* (Argelander 1859) and by Ross (1926) and, therefore, attracted the attention of many teams worldwide (Wilson 1953; Landolt 1983; Leggett 1992; Fischer & Marcy 1992; Reid et al.

1995, among many others). In contrast to G 264–012, Gl 393 was extensively monitored in search for exoplanets with RV (Isaacson & Fischer 2010; Bonfils et al. 2013; Butler et al. 2017; Grandjean et al. 2020), direct imaging (Masciadri et al. 2005; Lafrenière et al. 2007; Nielsen & Close 2010; Biller et al. 2013; Naud et al. 2017), and even radio (Bower et al. 2009; Harp et al. 2016).

For the two stars, we collected the photospheric parameters effective temperature T_{eff} , surface gravity $\log g$, and iron abundance $[\text{Fe}/\text{H}]$ from Passegger et al. (2019), which match those from other determinations (Lépine et al. 2013; Gaidos et al. 2014; Terrien et al. 2015; Rajpurohit et al. 2018; Passegger et al. 2018). Their metallicities are widely accepted to be roughly solar (see also Alonso-Floriano et al. 2015 and Dittmann et al. 2016). However, the *Gaia* DR2 T_{eff} value of G 264–012, of over 3800 K (Gaia Collaboration et al. 2018), is affected by systematics and does not agree with other literature determinations.

The stellar bolometric luminosities L_* , radii R_* , and masses M_* were taken from Schweitzer et al. (2019). New, more accurate, L_* values were computed by Cifuentes et al. (2020). Together with the T_{eff} of Passegger et al. (2019), the Stefan-Boltzmann law, and the empirical mass-radius relation from M-dwarf eclipsing binaries of Schweitzer et al. (2019), we re-determined R_* and M_* from these new L_* , but they differ by less than 2% from the values of Schweitzer et al. (2019), which is well within the uncertainties. For consistency with previous CARMENES works, we hereafter used the values of Schweitzer et al. (2019), which also agree with previous determinations in the literature (e.g. Dittmann et al. 2014; Newton et al. 2016).

To determine the parameters above, we assumed that the two stars are single (i.e. have no brown dwarf or stellar companion at close separations). For G 264–012, Janson et al. (2014) ruled out the presence of companions with $\Delta z' \gtrsim 7.5 \text{ mag}$ at angular separations greater than about 2 arcsec (and with $\Delta z' \gtrsim 4.0 \text{ mag}$ at $\rho > 0.5 \text{ arcsec}$), which translate into M and L dwarfs at about the substellar boundary at projected physical separations of over approximately 30 au (8 au). For Gl 393, having been observed with NACO at the VLT, NICI at Gemini-South, and Altair at Gemini-North (see above), the restrictions on the presence of very low-mass companions are even stronger. For example, in the first high-resolution imaging survey, Masciadri et al. (2005) excluded the presence of objects with $\Delta H \gtrsim 13 \text{ mag}$ (9.0 mag) at angular separations greater than about 2 arcsec (0.5 arcsec), which translate into (non-young) L and T dwarfs with masses of a few hundredths of M_{\odot} at projected physical separations of over approximately 14 au (3.5 au). Even stronger restrictions were imposed by complementary adaptive optics observations in CH_4 band at close separations, down to only 2.5 au, by Lafrenière et al. (2007) and Biller et al. (2013) and with seeing-limited imaging at wide physical separations, of 500–1000 au, by Naud et al. (2017).

All previous imaging surveys assumed a very young age for Gl 393 and, consequently, claimed to reach detection mass limits of a few Jupiter masses. With pre-*Gaia* data, Zuckerman et al. (2011) and Malo et al. (2013) assigned Gl 393 to the AB Doradus moving group. Previously, it was also proposed as a member of the Local Association (also known as Pleiades Moving Group; Montes et al. 2001, and references therein), an association that encompasses several moving groups, including AB Doradus (López-Santiago et al. 2006). The estimated age for the Local Association members ranges from 20 Ma to 300 Ma (López-Santiago et al. 2009), while AB Dor in particular has a better constrained age similar to that of the Pleiades open cluster (100–125 Ma; Luhman et al. 2005). Therefore, ages in the in-

¹ <https://reddots.space/>

Table 1. Stellar parameters of G 264–012 and Gl 393.

| Parameters | G 264–012 | Gl 393 | References ^a |
|---|-----------------------|---|-------------------------|
| <i>Identifiers</i> | | | |
| Name | G 264–012 | Gl 393 | Gic71 / Gli69 |
| Alt. name(s) | NLTT 52122 | BD+01 2447, Ross 446 | Luy79 / Arg1859, Ros26 |
| Karmn | J21466+668 | J10289+008 | Cab16a |
| <i>Coordinates, basic photometry, and spectral type</i> | | | |
| α (J2000) | 21:46:41.25 | 10:28:54.91 | <i>Gaia</i> EDR3 |
| δ (J2000) | +66:48:12.1 | +00:50:15.9 | <i>Gaia</i> EDR3 |
| G (mag) | 11.7531 \pm 0.0028 | 8.6760 \pm 0.0028 | <i>Gaia</i> EDR3 |
| J (mag) | 8.837 \pm 0.021 | 6.176 \pm 0.021 | 2MASS |
| Spectral type | M4.0 V | M2.0 V | AF15 |
| <i>Distance and kinematics</i> | | | |
| d (pc) | 15.986 \pm 0.010 | 7.0375 \pm 0.0025 | <i>Gaia</i> EDR3 |
| $\mu_\alpha \cos \delta$ (mas a ⁻¹) | 392.47 \pm 0.071 | -602.992 \pm 0.024 | <i>Gaia</i> EDR3 |
| μ_α (mas a ⁻¹) | 206.812 \pm 0.062 | -731.882 \pm 0.021 | <i>Gaia</i> EDR3 |
| γ (km s ⁻¹) | -9.771 \pm 0.024 | +8.005 \pm 0.023 | Laf20 |
| U (km s ⁻¹) | -29.238 \pm 0.018 | -7.27 \pm 0.01 | This work |
| V (km s ⁻¹) | -17.089 \pm 0.023 | -27.79 \pm 0.02 | This work |
| W (km s ⁻¹) | -9.164 \pm 0.016 | -15.45 \pm 0.02 | This work |
| <i>Photospheric parameters</i> | | | |
| T_{eff} (K) | 3326 \pm 54 | 3579 \pm 51 | Pas19 |
| log g [cgs] | 4.85 \pm 0.06 | 4.88 \pm 0.07 | Pas19 |
| [Fe/H] (dex) | +0.10 \pm 0.19 | -0.09 \pm 0.16 | Pas19 |
| <i>Physical parameters</i> | | | |
| L (L_\odot) | 0.01066 \pm 0.00011 | 0.02687 \pm 0.00054 | Schw19 |
| R (R_\odot) | 0.305 \pm 0.011 | 0.426 \pm 0.013 | Schw19 |
| M (M_\odot) | 0.297 \pm 0.024 | 0.426 \pm 0.017 | Schw19 |
| <i>Rotation and activity</i> | | | |
| $v \sin i$ (km s ⁻¹) | ≤ 2.0 | ≤ 2.0 | Rein18 |
| P_{rot} (d) | 100 \pm 6 | 34.15 ^{+0.22} _{-0.21} | This work |
| pEW(H α) (Å) | +0.077 \pm 0.009 | -0.005 \pm 0.007 | Schö19 |
| log R'_{HK} | ... | -4.91 \pm 0.06 | This work |
| log L_X (erg s ⁻¹ cm ⁻²) | ... | 26.83 ^{+0.15} _{-0.11} | This work |

References. ^a 2MASS: [Skrutskie et al. \(2006\)](#); Arg1859: [Argelander \(1859\)](#); AF15: [Alonso-Floriano et al. \(2015\)](#); Cab16a: [Caballero et al. \(2016\)](#); *Gaia* EDR3: [Gaia Collaboration \(2020\)](#); Gic71: [Giclas et al. \(1971\)](#); Gli69: [Gliese \(1969\)](#); Laf20: [Lafarga et al. \(2020\)](#); Luy79: [Luyten \(1979\)](#); New16: [Newton et al. \(2016\)](#); Pas19: [Passegger et al. \(2019\)](#); Rein18: [Reiners et al. \(2018\)](#); Ros26: [Ross \(1926\)](#); Schö19: [Schöfer et al. \(2019\)](#); Schw19: [Schweitzer et al. \(2019\)](#).

terval 70–200 Ma were proposed for Gl 393 (cf. [Masciadri et al. 2005](#); [Lafrenière et al. 2007](#); [Biller et al. 2013](#); [Naud et al. 2017](#)).

For both G 264–012 and Gl 393, we recomputed galactocentric space velocities UVW as in [Cortés-Contreras \(2016\)](#). We used *Gaia* DR2 proper motions and parallaxes and absolute (cross-correlation function) radial velocities from [Lafarga et al. \(2020\)](#). We compare our new UVW velocities (Table 1) against those of other members of young stellar kinematic groups from [Montes et al. \(2001\)](#) in Fig. 1. The kinematics of G 264–012 match those of other members of the IC 2931 and Hyades superclusters ([Eggen 1958, 1991](#)), with estimated ages of 35–55 Ma ([Eggen 1995](#)) and 600 Ma ([Eggen 1958, 1998](#)), respectively. As expected, the new kinematics of Gl 393 is compatible with members of the Local Association and matches the typical UVW for AB Doradus ([Malo et al. 2013](#); [Gagné et al. 2018](#)). However, despite both objects being kinematically young, all youth (i.e. activity) indicators available to us suggest otherwise. They are slow rotators from the strict upper limit in $v \sin i$ of 2 km s⁻¹ imposed by [Reiners et al. \(2018\)](#). The rotation period measured from the photometric and spectroscopic analysis in this work (see

Sect. 4.3), of about 100 d and 34 d for G 264–012 and Gl 393, respectively, are well above the periods measured for objects with similar spectral type in the Praesepe open cluster ([Rebull et al. 2017](#)), whose age (670 Ma; [Douglas et al. 2019](#)) is similar to the Hyades supercluster. The H α line in high-quality, high-resolution optical spectra is in very faint emission or even absorption ([Jeffers et al. 2018](#); [Schöfer et al. 2019](#)).

As described in Sect. 4.4, we also measured the intensity of the Ca II H&K lines of Gl 393. Our mean activity level of log $R'_{\text{HK}} = -4.91 \pm 0.06$ (Table 1) is in good agreement with values published by [Astudillo-Defru et al. \(2017\)](#), log $R'_{\text{HK}} = -5.031 \pm 0.106$, and [Boro Saikia et al. \(2018\)](#), log $R'_{\text{HK}} = -4.92$, consistent with the aforementioned rotation periods for M dwarfs, and well below the log R'_{HK} saturation limit at about -4.0 ([Suárez Mascareño et al. 2016](#); [Astudillo-Defru et al. 2017](#)). There are no archival high-resolution spectra covering Ca II H&K for G 264–012.

Gl 393 was detected in the X-ray range by the *ROSAT* all-sky survey ([Voges et al. 1999](#)). We transformed its count rate

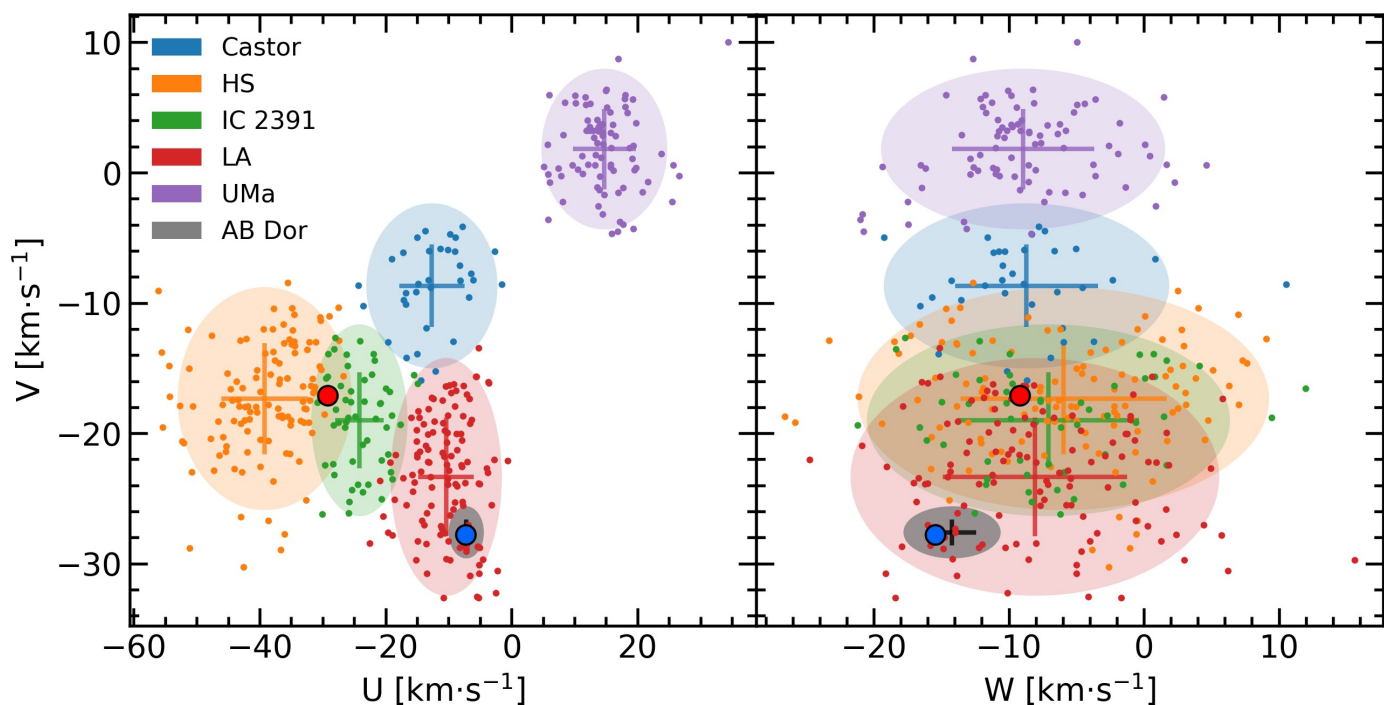


Fig. 1. UVW galactocentric space velocities of young moving group members in Montes et al. (2001, Castor, Hyades Supercluster, IC 2391 Moving Group, Local Association, Ursa Major, AB Doradus) along with G 264–012 (in red) and G 1393 (in blue). Crosses and ellipses correspond to the 1σ and 2σ values for each group, respectively. Over-plotted in grey are the typical UVW values and dispersion for AB Dor according to (Gagné et al. 2018).

and hardness ratio to flux as in González-Álvarez (2014) and, together with *Gaia* DR2 parallactic distance, X-ray luminosity. The measured $\log L_X$ value, also shown in Table 1, is much lower than the measured X-ray luminosity of members of moving groups younger than the Hyades supercluster (Stelzer et al. 2013). G 264–012 was not detected by *ROSAT*.

Both stars were analysed in the exhaustive multi-band photometric analysis of Cifuentes et al. (2020). While the bluest passband at which G 264–012 was detected was *B*, G 1393 has *GALEX FUV* and *NUV* measurements in the ultraviolet (Martin et al. 2005; Bianchi et al. 2014). However, its *FUV* magnitude of 21.57 ± 0.42 mag is at the survey detection limit and its *NUV*–*G_{RP}* colour of 11.542 ± 0.086 mag puts G 1393 in the locus of the least active (and oldest) stars in the colour-spectral type and colour-colour diagrams in Figs. A.1 and A.2 of Cifuentes et al. (2020). Its ultraviolet-optical and infrared colours are also above the expected value for objects younger than the age of the Hyades Supercluster (Findeisen et al. 2011).

3. Data

3.1. High-resolution spectroscopic data

G 264–012 was monitored only with CARMENES, whereas G 1393 was monitored also with another two instruments, namely HARPS and HIRES. The RV time series of the two stars and their uncertainties are listed in Tables B.1 and B.2. Table 2 shows a summary of the RVs used in this work and their overall quality, quantified by the mean formal RV uncertainties $\bar{\sigma}_{RV}$ and the root-mean-square (rms) scatter of the RVs around the mean.

Table 2. Number and quality of used RV observations.

| Instrument | N_{obs} | $\bar{\sigma}_{RV}$ [m s ⁻¹] | rms [m s ⁻¹] |
|------------------|------------------|---|-----------------------------|
| <i>G 264–012</i> | | | |
| CARMENES VIS | 159 | 1.7 | 4.3 |
| CARMENES NIR | 146 | 6.5 | 6.5 |
| <i>G 1393</i> | | | |
| CARMENES VIS | 84 | 1.5 | 2.3 |
| CARMENES NIR | 74 | 8.0 | 9.1 |
| HARPS | 180 | 1.1 | 2.3 |
| HIRES | 70 | 3.1 | 4.3 |

CARMENES. We observed G 264–012 and G 1393 as part of the CARMENES² guaranteed time observations survey to search for exoplanets around M dwarfs (Reiners et al. 2018). CARMENES is located at the 3.5 m telescope of the Calar Alto Observatory in Almería, Spain, and consists of two independent spectrographs, the visible channel (VIS; 5200–9600 Å, $R \approx 94\,600$) and the near-infrared channel (NIR; 9600–17 100 Å, $R \approx 80\,400$). Details on the instrument and its performance were given by, for instance, Quirrenbach et al. (2014, 2018), Trifonov et al. (2018), and Bauer et al. (2020). We observed G 264–012 from 19 June 2016 to 17 January 2020, spanning a total of 1310 days. We obtained 171 VIS and 168 NIR spectra with typical exposure times of 1800 s per spectrum. We rejected spectra with signal-to-noise ratios $S/N < 10$ (VIS: 6; NIR: 7) and spectra without simultaneous Fabry-Pérot drift measurement (VIS: 6; NIR: 4). As explained by Bauer et al. (2020), we further ex-

² <http://carmenes.caha.es>

cluded 11 spectra taken with CARMENES NIR prior to the achievement of thermal stability of the NIR channel. Thus, we were left with 159 VIS and 146 NIR spectra suitable for deriving high precision RVs.

G1393 was observed with CARMENES from 10 January 2016 to 17 June 2020, spanning a total of 1621 days, during which we obtained 84 VIS and 74 NIR spectra with typical exposure times of 580 s per spectrum. We excluded the first 8 NIR spectra in the time series for the same reason as above.

All CARMENES raw spectra were processed using *caracal* (Caballero et al. 2016; Zechmeister et al. 2014), which performs the basic spectral reduction process to obtain calibrated 1D spectra (wavelength calibration using Th-Ne, U-Ne, U-Ar, and Fabry-Pérot exposures, Bauer et al. 2015; simultaneous drift monitoring using Fabry-Pérot lamps, Schäfer et al. 2018; as well as spectrum extraction, Zechmeister et al. 2014). The RVs were obtained with *serval* (Zechmeister et al. 2018), a python code that uses a least-square-matching approach between each individual spectrum and a high S/N template, as described by Anglada-Escudé & Butler (2012). They were corrected for barycentric motion, secular perspective acceleration, instrumental drift, and nightly zero-point variations (Trifonov et al. 2018, 2020; Tal-Or et al. 2019).

HARPS. G1393 was also observed, from December 2003 to June 2017, with the High Accuracy Radial velocity Planet Searcher (HARPS, Mayor et al. 2003), a precise optical échelle spectrograph with a spectral resolution of $R \approx 110\,000$ installed at the ESO 3.6 m telescope at La Silla Observatory, Chile. We used 180 public HARPS RV datapoints corrected by Trifonov et al. (2020), who (i) computed RVs with *serval* that are, on average, more precise than the standard-pipeline DRS RVs by a few percent, (ii) accounted for nightly zero-point offsets that correct for HARPS systematic effects, and (iii) took into account the discontinuous RV jump caused by the fibre exchange in 2015.

HIRES. The High Resolution Echelle Spectrometer (HIRES; Vogt et al. 1994) is installed at the Keck I telescope in Hawai'i, USA. HIRES uses the iodine cell technique (Butler et al. 1996) to obtain RV measurements with a typical precision of a few m s^{-1} . We used 70 archival HIRES datapoints for G1393 to extend our time baseline from February 1997 to February 2014, which helped us with the analysis of possible long-period signals and to confirm the planetary signal found in the HARPS and CARMENES data sets. We used the HIRES data corrected by Tal-Or et al. (2019), who accounted for nightly zero-point offsets and an instrumental jump in 2004, which is an improvement over the original data reduction by Butler et al. (2017).

3.2. Photometric monitoring

We complemented our spectroscopic data with public and proprietary photometric light curves to study the rotation period of both stars. Variability caused by stellar activity, such as spots on the photosphere of M dwarfs, can lead to RV variations not attributable to planets (Baroch et al. 2020, and references therein).

We used archival ground-based photometry from ASAS, MEarth, and ASAS-SN, complemented with space-mission photometry from *Kepler* K2 and *TESS*. We also used unpublished data of the SuperWASP survey. In addition, we carried out our own photometric monitoring observations with the T90 telescope of the Sierra Nevada Observatory (OSN) and several

telescopes of the Las Cumbres Observatory Global Telescope (LCOGT) network. These data sets are summarised in Table 3, while the corresponding observing facilities and acquired data are described below.

3.2.1. Our observations

T90 at OSN. The T90 telescope at OSN³ in Granada (Spain) was used to obtain ground-based photometric observations of G 264–012 quasi-simultaneous with the spectroscopic ones. T90 is a 0.9 m Ritchey-Chrétien telescope equipped with a CCD camera VersArray 2k×2k with a resulting field of view (FOV) of $13.2 \times 13.2 \text{ arcmin}^2$. The camera is based on a high quantum efficiency back-illuminated CCD chip, type Marconi-EEV CCD42-4, with optimised response in the ultraviolet. Our set of observations, collected in Johnson *V* and *R* filters, consists of 78 epochs obtained between April 2019 and January 2020. Each epoch typically consisted of 20 observations of 80 s per night and per filter.

The resulting light curves were obtained via synthetic aperture photometry. Each CCD frame was corrected in a standard way for bias and flat field. Different aperture sizes were tested in order to choose the best one for our observations. A number of nearby and relatively bright stars within the frames were selected as check stars in order to choose the best ones to be used as reference stars (for further details Perger et al. 2019, see). The mean formal uncertainty, σ , of the data points of each night is of about 3.4 and 2.7 mmag in *V* and *R* bands, respectively.

LCOGT. Las Cumbres Observatory Global Telescope network⁴ (LCOGT, Brown et al. 2013) is a worldwide robotic telescope network that includes 0.4, 1.0, and 2.0 m telescopes. In particular, the 0.4 m telescopes are equipped with 2k×3k CCDs with a $19 \times 29 \text{ arcmin}^2$ FOV, while the 1.0 m telescopes are equipped with 4k×4k CCDs with a $27 \times 27 \text{ arcmin}^2$ FOV. We used one 0.4 m telescope located at Observatorio del Teide in Tenerife (Spain) and three 1.0 m telescopes: two located at Siding Springs Observatory (Australia) and one at McDonald Observatory (Texas, USA). We acquired data in the *V* filter only for G1393 in the period April–June 2020.

3.2.2. Photometric monitoring surveys

SuperWASP. The Super-Wide Angle Search for Planets⁵ (SuperWASP, Pollacco et al. 2006) consists of two robotic observatories, SuperWASP-North (La Palma, Spain) and SuperWASP-South (South Africa). Each has eight wide-angle cameras that simultaneously monitor the sky for planetary transits. The cameras, equipped with a 400 nm to 700 nm broadband filter, feed 2k×2k CCDs with a FOV of $7.8 \times 7.8 \text{ deg}^2$ per camera. No data on G 264–012 are available in the only SuperWASP public data release (DR1; Butters et al. 2010). Data used here were acquired for G1393 spanning the period from February 2008 to June 2014, including $\sim 74\,000$ useful observations distributed in clusters of ~ 100 days every season except in 2012. The data were reduced and detrended by the SuperWASP team following the algorithm described by Tamuz et al. (2005). This algorithm corrects the light curve for trends that manifest in a collection of simultaneously observed stars, which are generally attributed to atmospheric extinction and detector systematics.

³ <https://www.osn.iaa.csic.es/en>

⁴ <https://lco.global>

⁵ <https://www.superwasp.org>

Table 3. Photometric data sets for G 264–012 and Gl 393^a.

| Data set | Season | Filter | Δt (d) | N_{obs} | N_{nights} | rms (mmag) | P_{rot} (d) |
|------------------|-----------|----------------|-------------------|------------------|---------------------|---------------|-------------------------|
| <i>G 264–012</i> | | | | | | | |
| MEarth-1 | 2008–2009 | RG715 | 211 | 225 | 19 | 5.9 | ... ^b |
| MEarth-2 | 2011 | $I_{715-895}$ | 89 | 252 | 11 | 7.7 | ... ^b |
| MEarth-3 | 2011–2015 | RG715 | 1480 | 462 | 96 | 6.3 | ... ^b |
| ASAS-SN | 2015–2018 | V | 1316 | 222 ^c | 222 | 17.0 | 92.8 ± 0.8 |
| T90/OSN V | 2019 | V | 265 | 1413 | 78 | 5.4 | 99.7 ± 1.0 |
| T90/OSN R | 2019 | R | 265 | 1389 | 78 | 5.3 | 107.5 ± 1.2 |
| TESS | 2019–2020 | $T_{600-1000}$ | 244 | 50363 | 78 | 1.5 | ... ^b |
| <i>Gl 393</i> | | | | | | | |
| ASAS | 2001–2009 | V | 2969 | 358 | 358 | 14.0 | ... ^b |
| SuperWASP | 2008–2014 | $R_{400-700}$ | 2321 | 74021 | 445 | 7.6 | ... ^b |
| Kepler/K2 | 2017 | $K_{493-897}$ | 78 | 3393 | 78 | 0.6 | 34.0 ± 0.1 |
| LCOGT 1.0 m | 2020 | V | 72 | 181 | 38 | 7.9 | ... ^b |
| LCOGT 0.40 m | 2020 | V | 40 | 301 | 31 | 41.4 | ... ^b |

Notes. ^a The table header shows the data set identifier, the season, the filter used, the time span (Δt) of the observations, the number of individual observations (N_{obs}), the number of nights (N_{nights}), the rms of the residuals after removing the strongest signal in each data set, and the rotation period (P_{rot}) estimation with formal error bars. ^b Since no significant signal is found, tabulated rms is determined on the original time series. ^c Observations binned to one data point per night.

MEarth. The MEarth⁶ project consists of two robotically controlled telescope arrays devoted to monitoring thousands of M-dwarf stars (Berta et al. 2012). Since 2008, the MEarth-N (North) telescope array observes from the Fred Lawrence Whipple Observatory on Mount Hopkins (USA). This array consists of eight identical 0.4 m robotic telescopes ($f/9$ Ritchey-Chrétien Cassegrain), each equipped with a 2k \times 2k CCD camera, FOV of 26 \times 26 arcmin², sensitive to red optical and near-infrared light. MEarth has generally used an RG715 long-pass filter, except for the 2010–2011 season when an $I_{715-895}$ interference filter was used. In the case of G 264–012, three time series are available from the seventh data release, MEarth DR7, all collected with MEarth-N telescope T3. We dubbed them MEarth-1 (October 2008 to May 2009), MEarth-2 (March to June 2011), and MEarth-3 (October 2011 to November 2015).

ASAS-SN. The All-Sky Automated Survey for Supernovae⁷ (ASAS-SN) project (Kochanek et al. 2017) currently consists of 24 telescopes distributed on six different sites around the globe. Each station consists of four 14 cm aperture Nikon telephoto lenses, each with a thermo-electrically cooled, back-illuminated, 2k \times 2k, Finger Lakes Instruments ProLine CCD camera with a wide FOV of 4.5 deg². Only one data set, for G 264-012, was publicly available. This data set consisted in 601 useful V-band data points distributed over 222 nights during the period 2015–2018.

ASAS. The All-Sky Automated Survey⁸ project (ASAS, Pojmanski 1997) has been monitoring the entire southern, and part of the northern, sky since 1997. It consists of two observing stations, at Las Campanas Observatory in Chile (ASAS-3 from 1997 to 2010, ASAS-4 since 2010) and Haleakalā Observatory in Hawai‘i (ASAS-3N since 2006). Both are equipped with two

wide-field instruments observing simultaneously in the V and I bands. We retrieved 358 useful ASAS-3 V measurements for Gl 393 taken in the period between May 2001 and July 2009.

Kepler. Gl 393 was observed by the Kepler Space Telescope operating under the K2 mission⁹ (Howell et al. 2014) during campaign 14 from 2 June to 19 August 2017 with the long-cadence time resolution of ~ 30 min. The photometric light curves were retrieved from the Mikulski Archives for Space Telescopes¹⁰ (MAST). We used the pre-search data conditioning (PDC) light curves that are derived from processing the single aperture photometry (SAP) light curves by fitting co-trending basis vectors created from the stars in the same sector, camera, and CCD, to remove instrumental systematic variations and other perturbations such as pointing drifts, focus changes, gaps, or outliers. After removing outliers, mainly small flares, we reduced the number of 3537 useful data points to 3393.

TESS. G 264–012 was observed with a 2 min cadence by TESS in sectors S16 and S18 (cameras 2 and 3) in 2019 from 12 September to 6 October and 3 November to 26 November, respectively, and in sector S24 (camera 4) in 2020 from 15 April to 12 May¹¹. As in the case of Gl 393 and Kepler, we used the PDC light curves retrieved from MAST, which are optimised to search for exoplanet transits. The PDC light curves have 16 812 (S16), 15 334 (S18), and 18 217 (S24) useful points each. The three panels in Fig. 2 show the target pixel files (TPFs) and SAP apertures used in sectors S16, S18, and S24. We used tffplotter¹² (Aller et al. 2020), which overplots Gaia DR2 (Gaia Collaboration et al. 2018) sources in the nearby region. No objects down to 6 mag fainter (less than 0.4 % in flux) in G than G 264–012

⁹ <https://keplerscience.arc.nasa.gov>

¹⁰ <https://mast.stsci.edu/portal/Mashup/Clients/Mast/Portal.html>

¹¹ <https://heasarc.gsfc.nasa.gov/cgi-bin/tess/webtess/wtv.py?Entry=G+264-012>

¹² <https://github.com/jlillo/tffplotter>

⁶ <https://www.cfa.harvard.edu/MEarth>

⁷ <https://asas-sn.osu.edu>

⁸ <https://www.astrouw.edu.pl/asas>

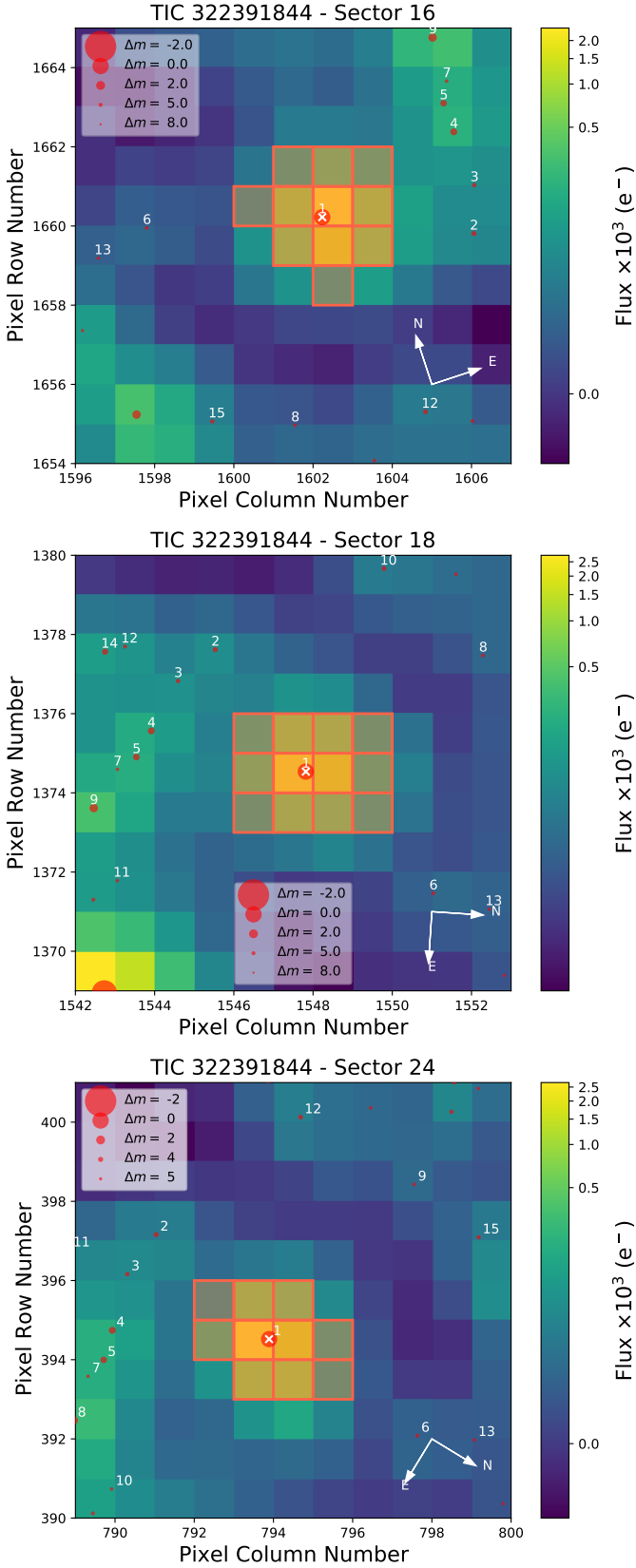


Fig. 2. TESS target pixel files of G 264–012, marked with a cross at the centre of the plot, in sectors 16 (left), 18, and 22 (right). Red points represent *Gaia* DR2 sources down to 6 mag fainter in *G* than G 264–012. The orange regions enclose the different pixel masks used to extract the single aperture photometry. *TESS* pixel size is about 21 arcsec.

are visible in the *TESS* SAP photometric apertures. *TESS* observed G1 393 in sector S35 during its extended mission between 9 February and 7 March 2021 with camera 1¹³.

4. Analysis and results

4.1. Signals in radial velocity data

To search for periodic signals, we computed the generalised Lomb-Scargle periodogram (Zechmeister & Kürster 2009) and determined the false alarm probabilities (FAP), as illustrated by Figs. 3 and 4. We considered a signal significant if its peak lies above the line for FAP = 0.1 % (i.e. with a FAP < 0.1 %). Significant signals were fitted and pre-whitened using Keplerian models. We continued searching in the pre-whitened RV data until no further significant signals were found.

We used the insights from the periodogram analysis to apply more sophisticated models to the RV data. Those models include planetary signals in the form of Keplerian orbits as well as the usage of Gaussian Processes (Rasmussen & Williams 2006) to mitigate the influences of stellar noise. These processes use a certain covariance function which is fitted to the autocorrelation function of the RV data. In exoplanetary science, some of those so-called kernel functions consist of a periodic component, indicating the variation introduced by the rotating star, and an exponential decay which measures the stability over time of the signal (Foreman-Mackey et al. 2017; Bauer et al. 2020; Toledo-Padrón et al. 2021). We chose the commonly used quasi-periodic kernel (Haywood et al. 2014; Rajpaul et al. 2015; Angus et al. 2018; Nava et al. 2020; Gilbertson et al. 2020; Toledo-Padrón et al. 2021) as shown here,

$$K_{QP}(\tau) = h^2 \exp\left(-\frac{\tau^2}{2\lambda^2} - \frac{1}{2w^2} \sin^2\left(\frac{\pi}{P}\tau\right)\right), \quad (1)$$

which introduces the four hyper-parameters h , a parameterisation of the signals amplitude in m s^{-1} , a period P_{rot} , describing the variability, the decay time of the correlation λ , and a factor w relating those two timescales (Perger et al. 2021a). Together with the parameters of a Keplerian orbit (semi-amplitude K , orbital period P , time t_c), offsets for the individual data sets μ , and additional jitters σ , we minimise the likelihood function by exploring the parameter space with a Markov Chain Monte Carlo (MCMC), using the emcee code (Foreman-Mackey et al. 2013) and the python-based george code (Ambikasaran et al. 2015). A model is significantly preferred if the difference in log-likelihood exceeded $\Delta \ln \mathcal{L} = 15$, in the sense that the higher the difference the higher the significance. A difference of $\Delta \ln \mathcal{L} < 5$ is considered noise. For a detailed discussion on the usage of this statistics for model comparison see Baluev (2013), and for an example implementation of this procedure see Perger et al. (2019).

4.1.1. G 264–012

Using our approach, we found that the G 264–012 CARMENES VIS RVs support the presence of three signals ($P_b = 2.30$ d, $P_c = 8.05$ d and $P_d = 92.70$ d; see panels (a–c) in Fig. 3). The two highest peaks are also found in the CARMENES NIR data, at 215.6 d (probably related with twice P_d in the VIS channel, considering the frequency resolution of 0.00076 c d^{-1} corresponding to our RV data set, given by the time span of

¹³ <https://heasarc.gsfc.nasa.gov/cgi-bin/tess/webtess/wtv.py?Entry=G1+393>

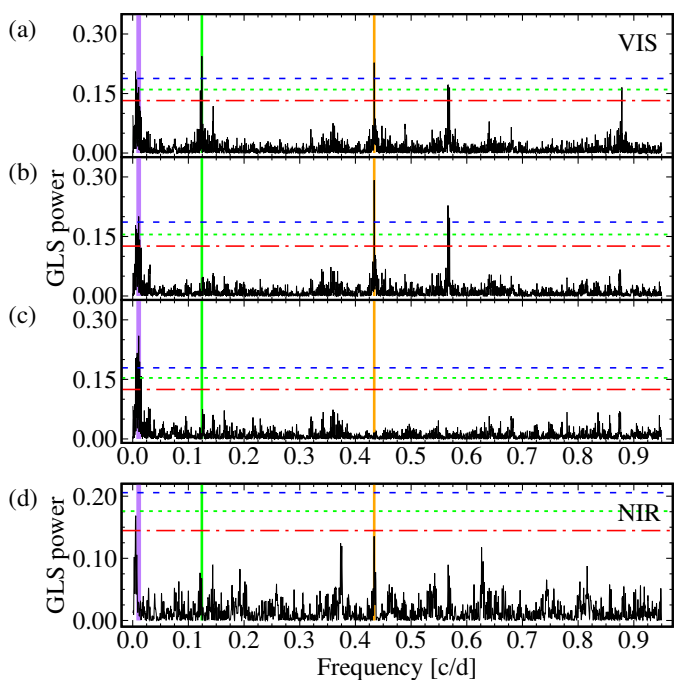


Fig. 3. GLS periodograms of G 264–012 RVs. *Panel (a)*: CARMENES VIS channel data. *Panels (b) and (c)*: residuals after pre-whitening the 8.05 and the 2.30 d periods, respectively. *Panel (d)*: CARMENES NIR channel data. In the four panels, dashed vertical lines mark the signals at 92.70 d (purple), 8.05 d (green), and 2.30 d (amber), while FAPs are indicated by horizontal lines: 10 % (red dash-dotted), 1 % (green dotted), 0.1 % (blue dashed).

Table 4. Log-likelihood $\ln \mathcal{L}$ for different RV models for G 264–012 and G1 393. Black font indicates the preferred solution

| N_{planets} | G 264–012 | | G1 393 | |
|----------------------|-----------|--------|--------|--------|
| | no GP | GP | no GP | GP |
| 0 | –456.4 | –424.1 | –807.6 | –727.4 |
| 1 | –443.0 | –422.6 | –799.6 | –706.8 |
| 2 | –422.6 | –393.7 | –798.6 | –705.4 |
| 3 | –413.4 | –389.5 | ... | ... |

$\Delta T = 1316$ d, see Sect. 3.1) and 2.30 d (same as P_b), though none of them were significant, as shown in panel (d) of Fig. 3.

A comparison of $\ln \mathcal{L}$ can be found in Table 4. The values show that a 2-planet + GP model is the preferred one. They also indicate that modelling the long period signal P_d with a Gaussian process instead of a Keplerian fit was highly preferred. This hinted towards stellar activity as the origin for the 92.70 d signal, but we gathered more evidence for this hypothesis in Sects. 4.2, 4.3, and 4.4, where we analyse photometric data and spectroscopic activity indicators in G 264–012. These indicators show indeed that this long-period signal is most probably due to activity. In Sect. 4.5, we study the system with a combined analysis with Gaussian Processes.

4.1.2. G1 393

The GLS periodograms for individual instruments, as well as the combined RV data set, of G1 393 can be seen in Fig. 4. In the HIRES (panel a) and HARPS (panel c) data sets, we found significant periods at 45.6 and 38.5 d, respectively, which appear

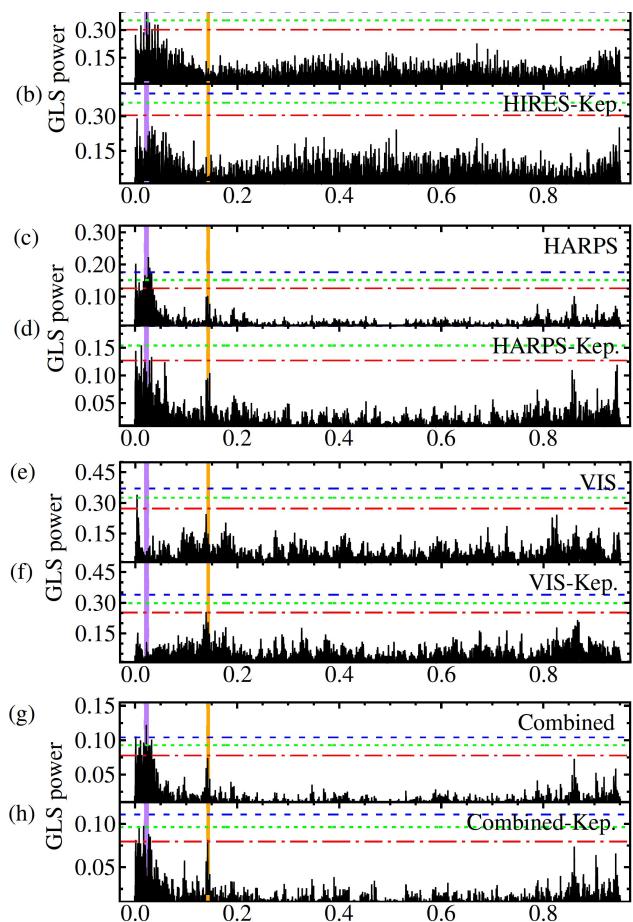


Fig. 4. GLS periodograms for G1 393: *Panel (a)*: HIRES data, and *Panel (b)*: HIRES data residuals after pre-whitening the highest peak with a Keplerian fit. *Panels (c), (d)*: HARPS data (panel descriptions as in those for HIRES), *Panels (e), (f)*: CARMENES VIS channel data, and *Panels (g), (h)*: combined data set. FAPs as in Fig. 3. Vertical dashed lines mark the highest peak found in the combined data (purple) and the highest peak after pre-whitening the GP (orange).

within a forest of low frequency peaks. In the VIS channel data of CARMENES, no significant signal was found (panel e). The highest peak represents a period of 302 d and reaches a FAP of 0.5 %. When combining all data sets (panel g), we found a significant period at 45.5 d, again within a forest of low-frequency peaks. After fitting and subtracting a Keplerian signal to the respective frequencies, we did not find a formally significant peak in any individual (panels b, d, and f) or in the combined (panel h) data set. However, we noticed the presence of a relatively high FAP (≈ 10 %) signal at 7.2 d in the VIS channel and at 7.0 d in the HARPS data and in the combined data. The signal is not seen in the HIRES data probably because of its higher rms scatter.

To investigate the stability of this second isolated frequency, we split the HARPS data set into two chunks of 90 data points each and repeated the periodogram analysis. We found the signal at around 7.0 d to be present in both HARPS subsets, while the forest of peaks around 38 d was highly variable and disappeared in the second HARPS subset. We also found the forest in the CARMENES data, but with a FAP barely below 10 %. Thus, we attributed the power seen at low frequencies in the periodograms to stellar activity, which is variable over time.

The complex nature of stellar activity hinders any signal search based on classical Keplerian pre-whitening approaches. Instead, we fit a Gaussian process (GP) with a quasi-periodic

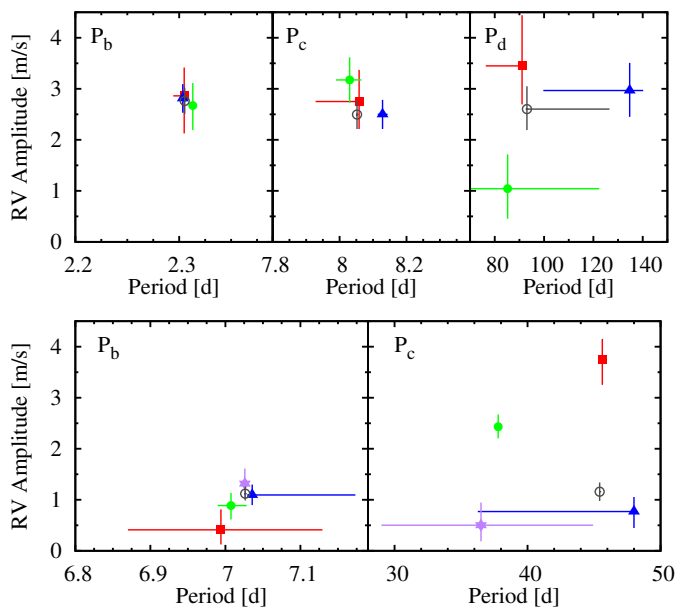


Fig. 5. *Top panels.* Period-amplitude diagrams of the Keplerian fits for the three signals in the G 264–012 RV data set split into seasons: 2016–17 (red squares), 2018 (green points), 2019 (blue triangles), and all data (grey circle). *Bottom panels.* Same as the top panels but for the Gl 393 RV data set split into subsets: HIRES (2008–2013; red squares), HARPS subset 1 (2003–2014; green points), HARPS subset 2 (2014–2017; blue triangles), CARMENES VIS (2016–2019; purple star), all data (grey circle).

kernel to the combined RV data set of CARMENES, HARPS, and HIRES. We tested several models against the Null model (no signals): a number of Keplerian models (around 7.0 d), a GP, and combined Kepler+GP.

As shown in Table 4, the GP is highly preferred over a Keplerian fit. Its significance also continuously increases with time when the RV points are sequentially added to the fit, showing that the RV data is dominated by complex magnetic activity. However, as we added additional RV data, the GP activity model alone is not enough to fit the data. When the combined RV data was corrected with the GP model (see panel g of Fig. 4), a significant (FAP = 0.1 %) signal was found at 7.0 d.

The $\ln \mathcal{L}$ comparison resulted in a highly preferred fit when a one-planet Keplerian model was combined with the GP, with subsequent addition of planets resulting in negligible improvement (see also Table 4). Hence, the signal found around 7.0 d was ascribed to be of planetary origin. Nevertheless, we investigated the photometric data and spectral activity indicators and provide our results in Sects. 4.3 and 4.4, respectively, where we show that the origin of the other signals is most probably due to activity.

4.2. Temporal and chromatic coherence

Testing the temporal and chromatic coherence of signals is a powerful tool to distinguish planetary Doppler signals from stellar activity with RV data alone (Bauer et al. 2020). In practice, these tests are often difficult to conduct because they require a large amount of RV data, especially in the case of low amplitude signals.

4.2.1. G 264–012

We started by analysing the temporal coherence of all three signals found in the VIS channel data of G 264–012. We split the VIS data set into seasons, where RVs taken during 2016 and 2017 were treated as one season because the sampling was too sparse to reliably fit three Keplerian orbits to each single season. The data taken during 2018 and 2019, however, were dense enough to treat them independently, as shown in Fig. 5, top panel. The two signals found at $P_b = 2.30$ d and $P_c = 8.05$ d were relatively stable in amplitude and period between different observing seasons, strengthening the planetary origin hypothesis. However, the signal at $P_d = 92.70$ d was variable in both amplitude and period over different seasons. Especially during the 2018 season the signal almost vanished in the RV data, which is a strong indication for variability due to stellar activity (cf. Bauer et al. 2020).

Chromatic coherence was difficult to test in G 264–012 because we lacked sufficient precision for the low amplitude signals to be seen with CARMENES NIR. Nonetheless, at least for the shortest period signal at $P_b = 2.30$ d, we could carry out a chromatic test of indicative character. We fixed the period to the one found with the VIS channel and fit both VIS and NIR RV data sets independently with a circular Keplerian orbit. Both fits yielded consistent RV semi-amplitude results, K , both in CARMENES VIS and NIR ($K_{\text{VIS}} = 2.76 \pm 0.26 \text{ m s}^{-1}$, $K_{\text{NIR}} = 1.88 \pm 1.20 \text{ m s}^{-1}$), as expected from a planetary signal origin.

4.2.2. Gl 393

Testing chromatic and temporal coherence in the RV data of Gl 393 was also challenging, especially for the signal at 7.0 d, as its amplitude is only about 1 m s^{-1} . To test the temporal coherence, we analysed the HIRES, HARPS, and CARMENES VIS data sets independently, but split the large HARPS set into two subsets of 90 data points each. In each data set, we fit both, a signal between 25 and 50 days and one at around 7.0 d.

The signal around 45.5 d (right panel in Fig. 5) decreased in amplitude over time. It exhibited an amplitude of about 4 m s^{-1} in the HIRES data and decreased to 2.5 m s^{-1} in the first HARPS subset before later vanishing completely in the second HARPS subset and the CARMENES data (in the last two cases the derived amplitude fell below the instrumental precision at around 1 m s^{-1}). The behaviour observed in this signal points towards variability due to stellar activity. The amplitudes and periods around 7.0 days derived from CARMENES and HARPS data are quite consistent, whereas the HIRES data yield a non-detection (possibly due to the larger rms and fewer RV data points). Nonetheless, the derived RV amplitudes of about 1 m s^{-1} are around the limit of a reliable detection from all subsets (see left panel of Fig. 5). We can, therefore, extract no information regarding the temporal coherence of the 7.0 d RV signal from this test.

Testing chromatic coherence in Gl 393 is beyond what can be achieved with the current RV data set. This is the case because CARMENES did not observe Gl 393 long enough to reach the required precision with its NIR channel.

4.3. Search for variability in photometric data

In single M dwarfs, brightness variations are caused by starspots, or other activity structure on the stellar surface, moving across the stellar disc by rotation. The two host stars, G 264–012 and

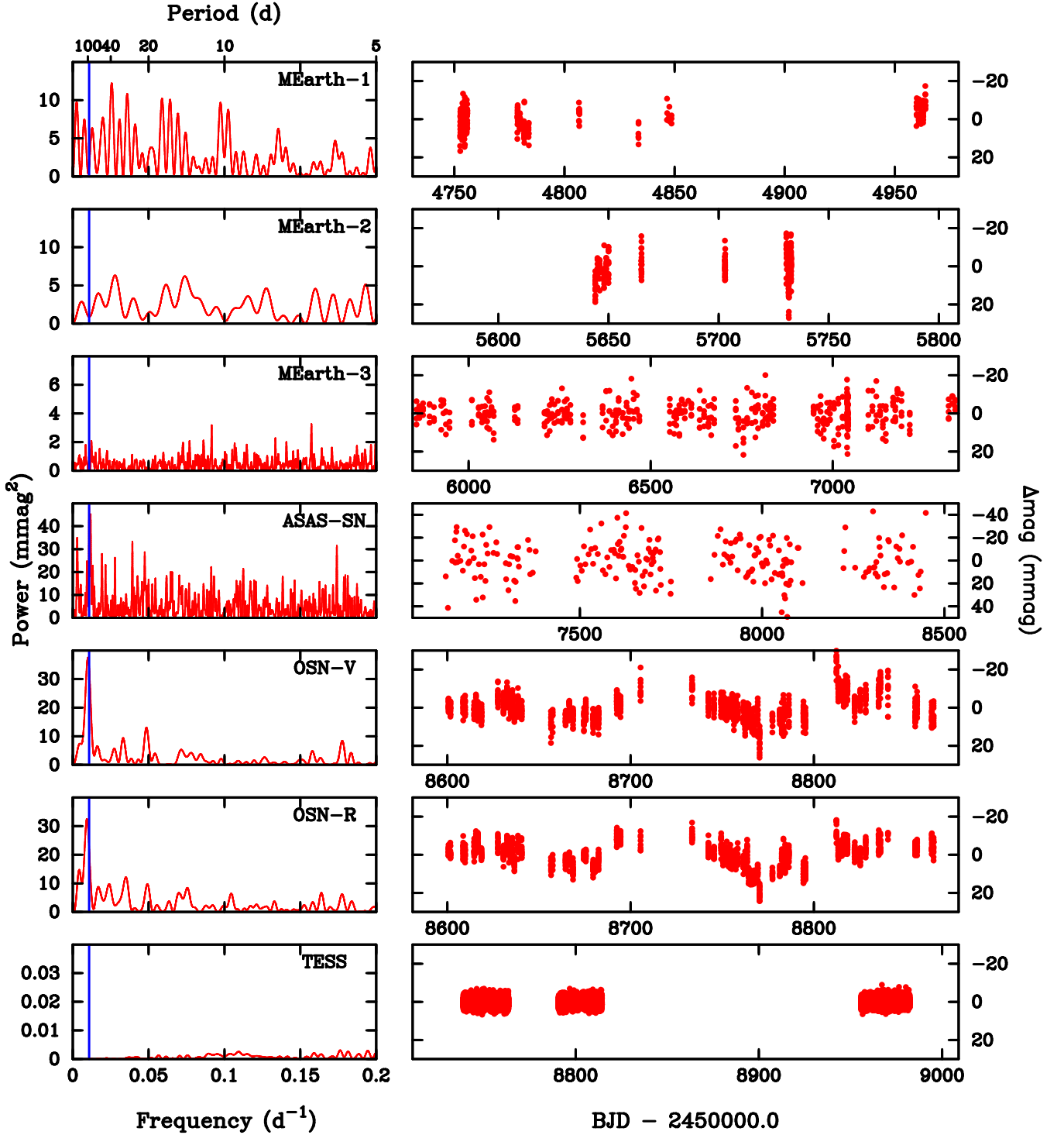


Fig. 6. Analysis for periodicity using available photometric data sets of G 264–012. *Left panels:* power spectra. *Right panels:* time series. The vertical blue solid line in the left panels indicate the period of 92.7 d derived in the RV time series.

G1 393, were monitored in photometric surveys in search for these variations to determine their rotation periods.

Newton et al. (2016) analysed the first 230 MEarth data points of G 264–012 collected in the 2010 campaign. They determined $P_{\text{rot}} = 48.51$ d with $A = 9.9 \pm 4.1$ mmag but considered it a ‘non-detection or undetermined detection’ (source type N) with a ‘bright contaminant’ (contamination flag 1). Díez Alonso et al. (2019) extended the analysis to 790 MEarth data points col-

lected in the campaigns 2010, 2011, and 2014, but did not find a reliable period, either.

The ASAS light curve of G1393 was also investigated by Díez Alonso et al. (2019). In spite of the 413 data points over 8.636 a, they again did not find any reliable period. Later, Reinhold & Hekker (2020) determined $P_{\text{rot}} = 35 \pm 13$ d with a variability range of 0.49 % using ultra-precise *Kepler* data collected

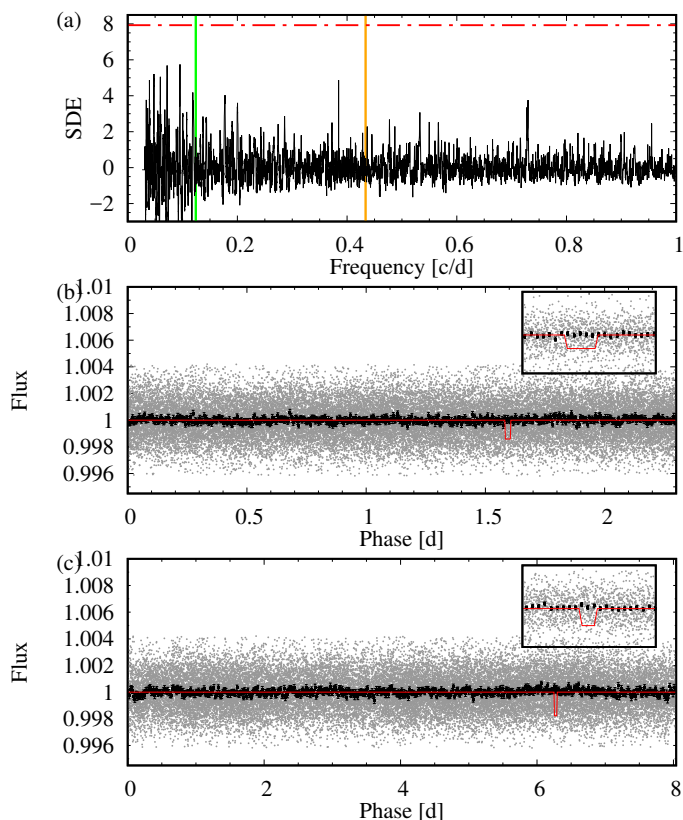


Fig. 7. *G 264–012:* Panel (a): transit search signal detection efficiency (SDE) as a function of frequency using the TLS algorithm. The red dashed-dotted horizontal line marks the 10% FAP, the vertical green and yellow lines mark the signals found in the CARMENES RV data at 8.05 d and 2.30 d, respectively. Panel (b): *TESS* data folded to the 2.30 d signal. *TESS* two minute cadence data (grey dots), phase binned *TESS* data (black squares), expected transit signal (solid, red line). Panel (c): same as panel (b) but for the 8.05 d signal.

during the K2 campaign 14 (between 31 May and 19 August 2017).

The undetermined period of G 264–012 and the large uncertainty in the G1393 rotation period led us to perform our own search for low-amplitude photometric variability, including a brand-new transit search. For the two stars, we carried the transit search with the transit least squares (TLS) algorithm (Hippke & Heller 2019), which is optimised for the detection of small planets with low signal to noise in large data sets, such as those supplied by *TESS* or *Kepler*. TLS evaluates a statistic, the signal detection efficiency (SDE), to identify transiting candidates. Typically, an $SDE = 8$ is equivalent to an $FAP \approx 10\%$.

4.3.1. G 264–012

We analysed all the available photometric data sets of G 264–012, including the new and contemporaneous measurements collected at OSN. The results are summarised in Fig. 6 and Table 3.

As Newton et al. (2016) and Díez Alonso et al. (2019), we did not find any significant periodicity in the frequency analysis of the MEarth data, whose periodogram shows a very low mean power level, suggesting a very low activity level during the epoch of these observations (2010–2015). However, the level of surface activity in G 264–012 increased after 2015. Although the ASAS-SN data set is noisier than MEarth ones, its periodogram shows power in the low-frequency region, with a main peak at fre-

quency $f = 0.01078 \text{ d}^{-1}$ ($P = 92.8 \text{ d}$, amplitude $A \approx 7.0 \text{ mmag}$), consistent with the long-period signal of 92.7 d detected in the RV time series. The same results were obtained after nightly binning the ASAS-SN time series. Furthermore, the analyses of the OSN photometric time series in both V ($P \sim 99.7 \text{ d}$) and R ($P \sim 107.5 \text{ d}$) filters were consistent with each other and with the ASAS-SN data set.

The *TESS* data set consists of a time series obtained during three sectors, S16, S18 and S24, with effective time spans of 24.7, 23.7 and 26.5 d, respectively, and a total time baseline of 244 d. In general, *TESS* SAP light curves are commonly affected by instrumental drifts, while the PDC ones are not. However, when creating the PDC light curves, low-amplitude, mid-term variations intrinsic to the star are also disturbed or even removed. In the case of G 264–012, the relatively long periodicity of about 90–100 d, the small amplitude of a few millimagnitudes, and the time gaps of nearly 60% of the baseline prevented us from detecting any rotational modulation in the *TESS* data. In particular, we imposed an upper limit of 0.15 mmag to the amplitude of the stellar variability remaining in the PDC light curve (Fig. 6), as given by the maximum level of the forest of peaks in the noise shown in its periodogram.

We used the george kernel (Ambikasaran et al. 2015) and a dynamic nested sampling with juliet (Espinoza et al. 2019) for a GP fit on the combined, nightly-binned, photometric data. Of the four GP hyperparameters of this kernel, the amplitude and harmonic complexity were individual for each data set, whereas the rotation period and decay timescale were shared by all of them.

After injecting a uniform P_{rot} prior between 1 and 200 d, we measured a posterior rotation period of $112.5^{+1.2}_{-1.5} \text{ d}$. We repeated the fit after discarding the MEarth and *TESS* data sets and keeping only the ASAS-SN and OSN sets, with the clearest signals, and found a consistent value with a smaller uncertainty, $P_{\text{rot,GP}} = 112.6 \pm 0.9 \text{ d}$.

Given the low amplitude of the photometric variability of G 264–012, of the order of the error bars of the individual data points, we were conservative in assigning a mean rotation period for the star of $100 \pm 6 \text{ d}$, as derived from the three values presented in Table 3.

We looked for transits in the *TESS* sectors. As illustrated by Fig. 7, no transit is evident from the SDE at the periods of 2.30 d and 8.05 d found in CARMENES RVs (Sect. 4.1). The position of the transits were computed from the RV solution, while the transit depths were estimated assuming a rocky and silicate composition (Zeng et al. 2019), as corresponding to hypothetical Earth-like planets. The expected transit depths were 1500 ppm for the 2.30 d signal and 1900 ppm for the 8.05 d signal. As a comparison, the *TESS* light curve has an rms of 654 ppm and error bars of typically 766 ppm.

4.3.2. G1393

The high-quality *Kepler* K2 light curve (see Sect. 4.5.2) was analysed in order to determine the rotation period of G1393. The light curve displays flares, as expected from a moderately active star, on top of significant quasi-periodic variations with time scales of tens of days and a long-term linear trend, probably of instrumental origin. Hence, we first linearly detrended the light curve and removed flares with a 3σ -clipping filter. Our frequency analysis, with the interactive computer package Period04 (Lenz & Breger 2005), which is based on algorithms similar to the Lomb-Scargle periodograms, resulted in a main periodicity of $P \sim 34.0 \pm 0.1 \text{ d}$. The amplitude of this variabil-

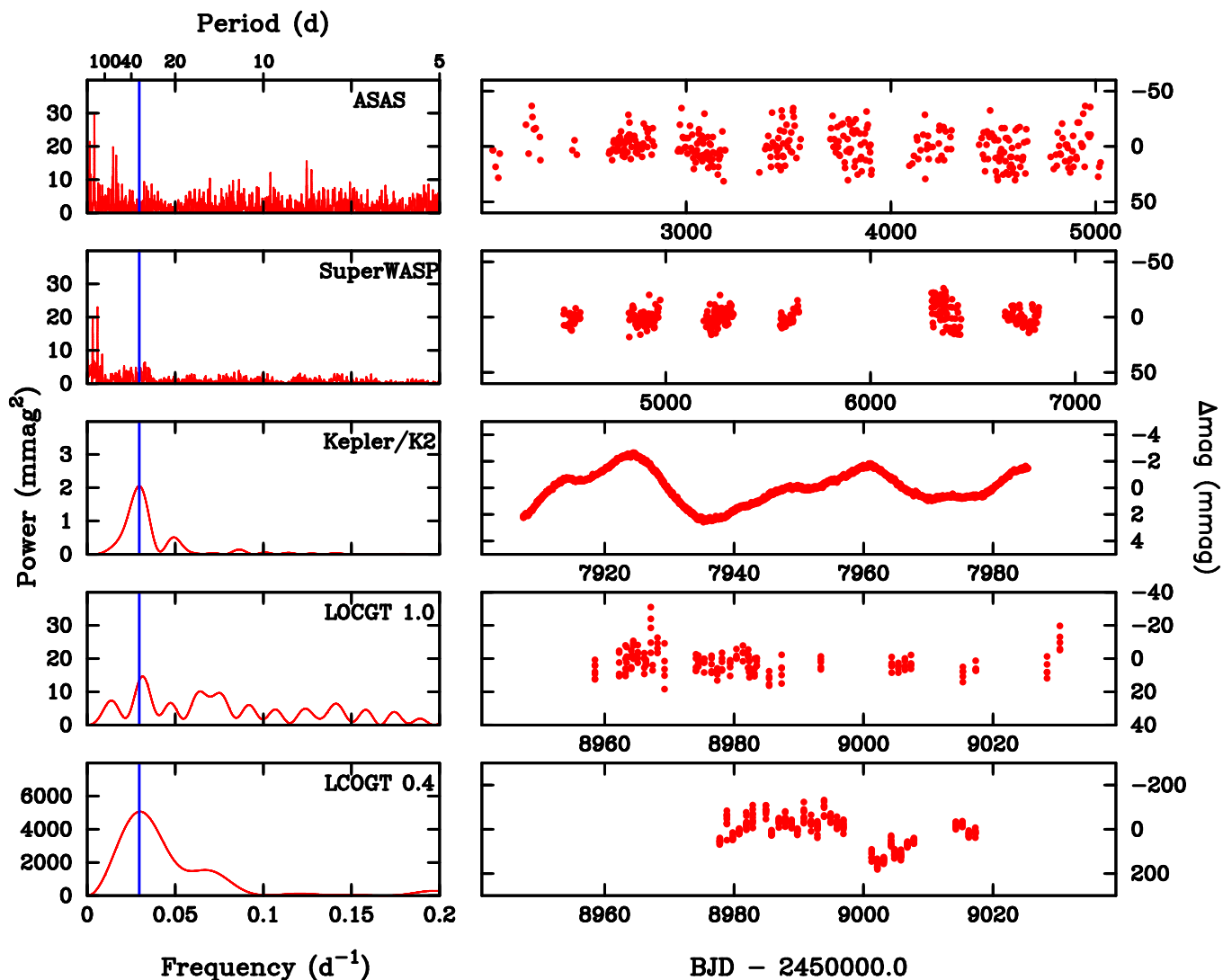


Fig. 8. Same as Fig. 6, but for Gl 393 and the period of 34.0 d derived from the *Kepler* K2 light curve.

ity is $A = 3.0 \pm 0.1$ mmag (full peak-to-peak amplitude), which we attributed to the rotation period of Gl 393. This is in good agreement with the determination of 35.1 ± 13.0 d by Reinhold & Hekker (2020). Furthermore, there is no sign of any peak at 7.0 d that could challenge the planetary origin of this signal.

As expected from the very small amplitude of the surface activity signal shown by the *Kepler* K2 light curve of Gl 393, we did not find any significant periodicity in the frequency analysis of the time series obtained from ground-based photometry alone (ASAS, SuperWASP, and LCOGT; see Fig. 8 and Table 3 for a summary). However, the combination of different data sets may improve the P_{rot} determination. Thus, we made joint fits with a quasi-periodic GP with different data set combinations. Probably due to the relatively large uncertainty of the ASAS and SuperWASP data with respect to the small amplitude of variability, the combination that led to the most robust P_{rot} determination was that of joining *Kepler*, LCOGT 1.0 m, and LCOGT 0.4 m, which resulted on a rotation period $P_{\text{rot}} = 34.15^{+0.22}_{-0.21}$ d (68 % confidence interval uncertainties), similar to that of Reinhold & Hekker (2020).

We performed a transit search in the available K2 data of Gl 393 (Fig. 9). For that, after detrending and flare-subtraction, we modelled and corrected the light curve with a GP with Matérn kernel prior to its analysis with TLS. The 7.0 d signal would produce a transit depth of 770 ppm assuming, as in G264-012, a terrestrial composition for the planet. Such a transit signal should be clearly visible in the K2 light curve, which has an rms of 35 ppm and error bars of typically 38 ppm. However, we do not find any evidence for a periodic dip.

4.4. Search for variability in the activity indicators

4.4.1. G 264–012

In addition to the photometric follow up, we also investigated a number of spectral line indices that are sensitive to photospheric or chromospheric activity. All of them were already successfully used, or recently suggested in the literature (Andretta et al. 1997; Martin et al. 2017; Schöfer et al. 2019; Fuhrmeister et al. 2019), to uncover stellar activity signals. We also used the several indicators, differential line width (dLW) and chromatic index (CRX) defined by Zechmeister et al. (2018) to gain further insights into

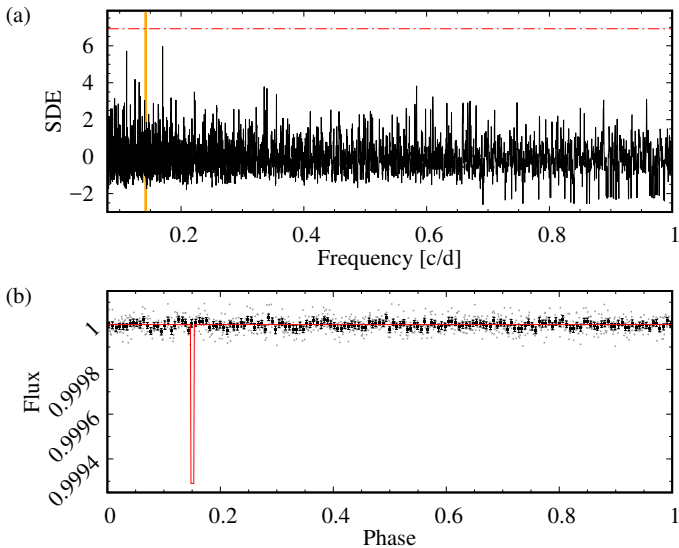


Fig. 9. G1393: *Panel (a)*: Transit search signal detection efficiency (SDE) as a function of frequency for K2 data. The horizontal dashed-dotted line marks the 10% FAP, while the vertical yellow dashed line marks the 7.0 d signal found in the RVs. *Panel (b)*: K2 data (grey) folded to the 7.0 d signal. Black dots are the binned K2 data, while the red line shows the simulated transit.

the nature of the signals found in the RVs and the photometry. In Fig 10, we present the GLS periodograms of all our activity indicators gathered for G 264–012.

Among the collected spectroscopic indicators, we found $H\alpha$ ($P = 92.4$ d), $He\ I\ 10833\ \text{\AA}$ ($P = 183.3$ d), $Pa\beta$ ($P = 215.7$ d), VIS CRX ($P = 339.4$ d), and NIR CRX ($P = 88.2$ d) to exhibit significant signals above the $FAP = 0.1\%$ level. The periods found in $H\alpha$ and NIR CRX match the signal $P_d = 92.7$ d found in the VIS channel RVs. Furthermore, $He\ I\ 10833\ \text{\AA}$ and $Pa\beta$ reflect the highest peak found in the NIR channel RVs (215.6 d) and are, thus, likely associated with P_d via a factor of 2, taking into account the frequency resolution of $0.00076\ \text{c d}^{-1}$ corresponding to our RV data set, from a time span of $\Delta T = 1316$ d (see Sect. 3.1). An even better agreement can be found if we assume that the true $P_{\text{rot}} \sim 100$ d for G-264-012, as follows from the photometric results listed in Table 3. That is, the frequency resolution is not enough to resolve between the two resulting values (215 d and $2P_{\text{rot}}$) in our periodograms. The signal of 339.4 d found in the VIS CRX periodogram is close to a one-year periodicity and therefore may represent an alias. Using all the evidence collected from photometry (i.e. ASAS-SN and OSN) and spectroscopic activity indicators, we concluded that the RV signal $P_d = 92.7$ d is linked to the rotational period of G 264–012.

4.4.2. G1393

We repeated the analysis of various activity indicators of G1393 and plot their periodograms in Fig. 11. Among all indicators, only the $H\alpha$ index in CARMENES ($P = 1130$ d) and HARPS ($P = 1500$ d), as well as the HARPS-dLW ($P = 4270$ d), show significant signals. The long periods found match neither the photometric rotation period of 34.0 d derived from K2 data nor the 7.0 d RV signal, but could instead hint at an activity cycle of many years (which would be consistent with the temporal coherence test of Sect. 4.2; see Díez Alonso et al. 2019 for a summary of photometric long-term cycles in M dwarfs).

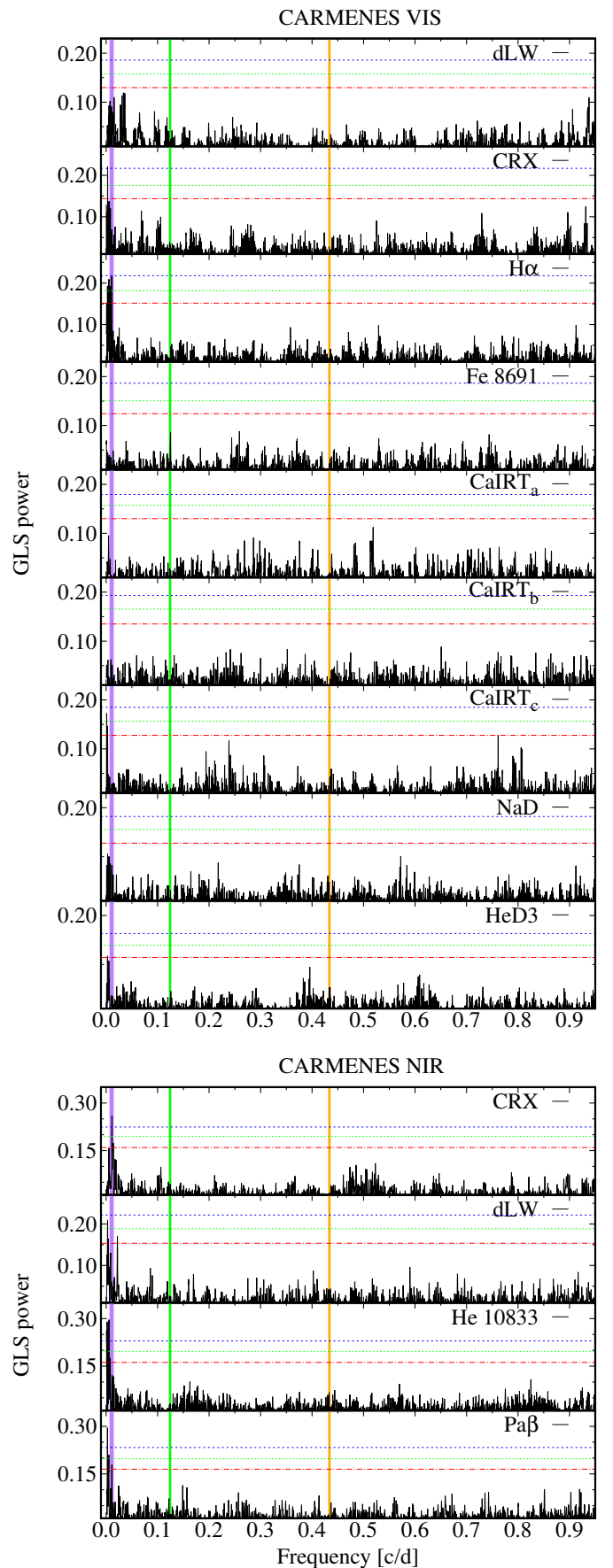


Fig. 10. GLS periodograms of CARMENES activity indicators of G 264–012 in the VIS (*top panels*) and NIR (*bottom panels*) channels. Horizontal FAP lines and vertical signal indications are the same as in Fig. 3.

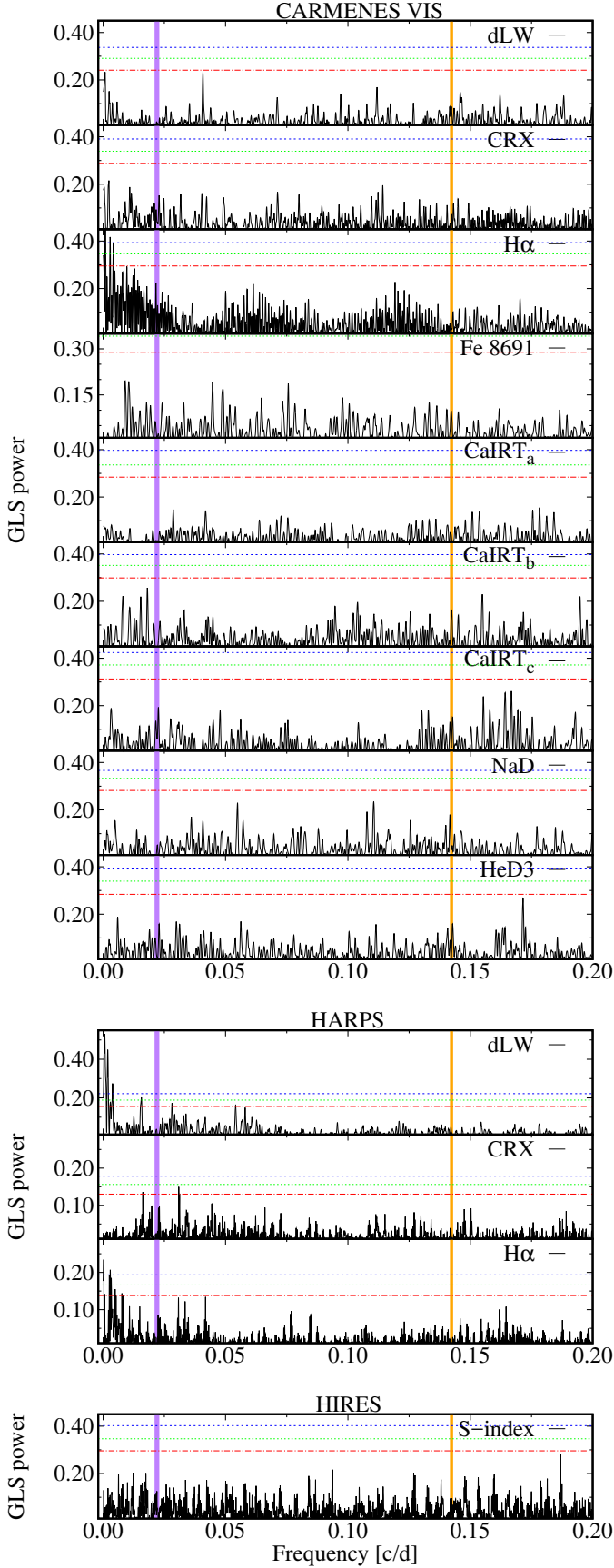


Fig. 11. GLS periodograms of CARMENES VIS, HARPS, and HIRES activity indicators for G1 393. Horizontal FAP lines and vertical signal indications are the same as in Fig. 4.

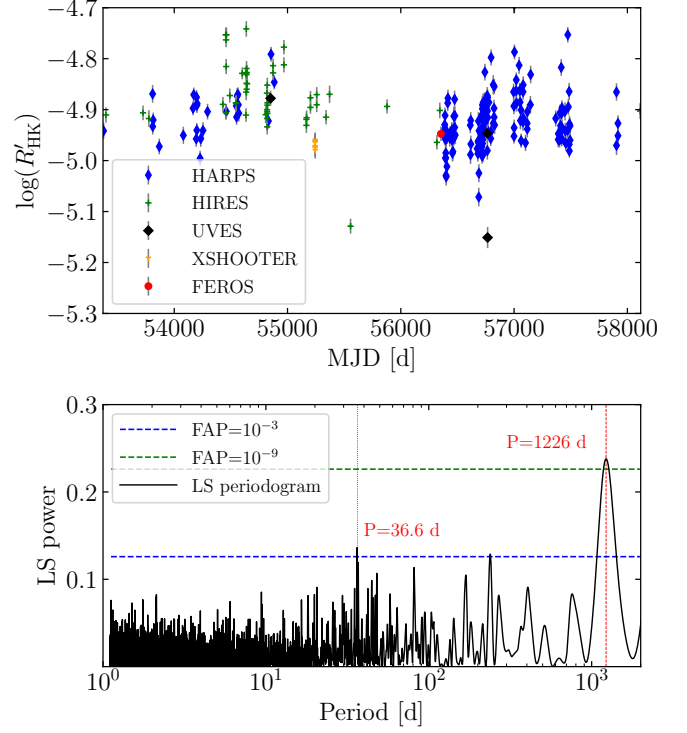


Fig. 12. *Top panel.* R'_{HK} time series of G1 393. The source of the archival data is denoted by the colour coding. *Bottom panel.* Generalised Lomb-Scargle periodogram of the R'_{HK} time series of G1 393. The dashed vertical lines denote the periods of the activity cycle ($P \approx 1226$ d) and stellar rotation ($P \approx 36.6$ d) determined from the R'_{HK} time series. FAP levels of 10^{-3} and 10^{-9} are displayed as horizontal lines.

Since the CARMENES spectral range does not include the Ca II H&K lines, we carried out an analysis of all available archival data covering this spectral region, namely the HARPS and HIRES spectra used in the RV analysis of this work (Sect. 4.1.2), 1 spectrum acquired by FEROS (Kaufer et al. 1999), 3 spectra from UVES (Dekker et al. 2000), and 10 from XSHOOTER (Vernet et al. 2011). In order to extract R'_{HK} from spectra acquired by all five instruments in a uniform manner, we rectified the spectra with a grid of PHOENIX spectra (Husser et al. 2013) by extracting a set of narrow band passes around both the H and K lines. The approach will be described in detail in an upcoming publication (Perdelwitz et al. in prep.). The top panel of Fig. 12 shows the resulting R'_{HK} time series. The smaller periodicity in the bottom panel of Fig. 12, with a period of $P = 36.6 \pm 1.9$ d, where the error was determined via a Monte Carlo approach, is in agreement with the stellar rotation period derived from *Kepler* K2 photometry (Section 3.2).

4.5. Gaussian process analysis of RV data

4.5.1. G 264–012

All indicators gathered (Sect 4.2 to Sect 4.4) point towards activity as origin for the RV signal found at a period of $P_d = 92.70$ d in G 264–012. There is, however, no indicator contradicting the planetary nature of the other two signals, $P_b = 2.30$ d and $P_c = 8.05$ d. In order to accurately determine their orbital parameters and masses, we account for stellar activity in our models. We choose a model with two circular Keplerian orbits (no evidence for eccentricity was found in these two very-short period planets, whose orbits should be almost certainly already circu-

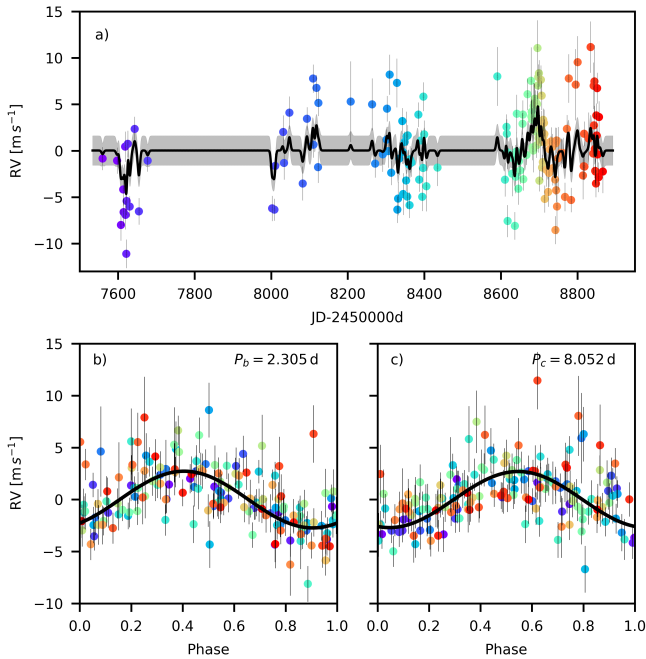


Fig. 13. G 264–012. *Panel a*): GP fit (black solid line) and 1-sigma uncertainties (grey area) to CARMENES VIS RVs (points colour-coded by JD). *Panels b*), *c*) show the phase-folded RVs after subtracting activity of the two planetary signals. Keplerian models (black solid lines) are overplotted.

larised, see Sect 4.1) for the planets combined with a Gaussian process (quasi-periodic kernel; see Eq. 1) for the activity signal.

We present the fits in Fig. 13, a summary of all parameters used in the model in Table 5 and the MCMC posterior distribution plot in the appendix in Fig. A.1. When subtracting the model from the VIS RV data we derived an rms of 2.22 m s^{-1} , which is consistent with the errorbars.

The model is very well constrained for the planetary parameters. The periodicity P and λ -timescale of the GP component are less clearly found. The first has indistinguishable solutions ($\Delta \ln \mathcal{L} < 5$) also for $P \sim 200$ days, which is why we set a prior with $P < 120$ days, leading to an estimation for the rotational period of 102 ± 4 days. Solutions for λ are not well constrained, showing probably a large variability of the spot lifetimes. We find $64 < \lambda < 166$ days, suggesting average spot lifetimes of $1 - 2.5 P_{\text{rot}}$ (Perger et al. 2021a).

4.5.2. Gl 393

Gl 393 has a rotational period of 34.0 d as derived from K2 photometry and in agreement with the periodicity of the Ca II H&K variability. Spot patterns seem to evolve rapidly, giving rise to a complex, activity driven RV variability. To derive the parameters of the planetary signal discovered in the RV data, activity modelling is crucial. We proceeded in the same manner as for G 264–012 and fitted a circular Keplerian model (no eccentric orbit solution was found to be significant from our analysis in Sect. 4.1) combined with a GP using a quasi-periodic kernel which accounted best for the evolving activity signal. The resulting fits to the data are presented in Fig. 14 and the parameters used when deriving the models are summarised in Table 6. The MCMC posterior distribution plot is shown in the appendix in Fig. A.2. When subtracting the model from the data

Table 5. G 264–012: priors, best likelihoods, and posterior distribution uncertainties of the combined planets plus activity fit to RVs and derived planetary parameters^a.

| Parameter | Prior | Posterior | Unit |
|----------------------------------|--|---------------------------------|-------------------|
| <i>Planets</i> | | | |
| P_b | $\mathcal{U}(1.5, 220)$ | $2.30538^{+0.00031}_{-0.00031}$ | d |
| K_b | $\mathcal{U}(0, 5 \sigma_{\text{RV}})$ | $2.72^{+0.28}_{-0.29}$ | m s^{-1} |
| $t_{c,b} - 2458000$ | $\mathcal{U}(0, 220)$ | $3.235^{+0.069}_{-0.073}$ | d |
| P_c | $\mathcal{U}(1.5, 220)$ | $8.0518^{+0.0034}_{-0.0034}$ | d |
| K_c | $\mathcal{U}(0, 5 \sigma_{\text{RV}})$ | $2.69^{+0.31}_{-0.30}$ | m s^{-1} |
| $t_{c,c} - 2458000$ | $\mathcal{U}(0, 220)$ | $4.40^{+0.24}_{-0.23}$ | d |
| <i>GP kernel hyperparameters</i> | | | |
| h | $\mathcal{U}(0, 5 \sigma_{\text{RV}})$ | $1.59^{+0.36}_{-0.36}$ | m s^{-1} |
| P | $\mathcal{U}(0, 120)$ | $102.2^{+4.2}_{-4.4}$ | d |
| λ | $\mathcal{U}(0, \sim 2800)$ | 96^{+70}_{-32} | d |
| w | $\mathcal{U}(0, 1)$ | $0.271^{+0.108}_{-0.089}$ | |
| <i>Instruments</i> | | | |
| σ | $\mathcal{U}(0, 3 \sigma_{\text{RV}})$ | $0.48^{+0.36}_{-0.36}$ | m s^{-1} |
| μ | $\mathcal{U}(\mu_1, \mu_2)$ | $0.02^{+0.53}_{-0.54}$ | m s^{-1} |
| <i>Derived</i> | | | |
| a_b | | $0.02279^{+0.00061}_{-0.00061}$ | au |
| $M_b \sin i$ | | $2.50^{+0.29}_{-0.30}$ | M_{\oplus} |
| S_b | | $20.5^{+1.1}_{-1.1}$ | S_{\oplus} |
| $T_{\text{eq},b}$ | | 587^{+16}_{-16} | K |
| a_c | | $0.0525^{+0.0014}_{-0.0014}$ | au |
| $M_c \sin i$ | | $3.75^{+0.48}_{-0.47}$ | M_{\oplus} |
| S_c | | $3.87^{+0.21}_{-0.21}$ | S_{\oplus} |
| $T_{\text{eq},c}$ | | 387^{+11}_{-11} | K |

Notes. ^a $\mu_1 = \overline{RV} - 3 \sigma_{\text{RV}}$, and $\mu_2 = \overline{RV} + 3 \sigma_{\text{RV}}$, with \overline{RV} and σ_{RV} , as the average and the rms of the RV time series, respectively.

we find an rms of 3.32 m s^{-1} for HIRES, 1.19 m s^{-1} for HARPS and 1.50 m s^{-1} for CARMENES VIS; all are consistent with the respective error estimates in each data set. All parameters are very well constrained, with the exception of the periodicity P which, resembling the results of the periodogram analysis, tends to vary between 30 and 50 days, and with a maximum likelihood for $P=35.0$ days. We calculate an average spot lifetime of $2 - 3 P_{\text{rot}}$ from the λ -hyperparameter.

5. Discussion

5.1. Comparison with other surveys

As discussed in Sect. 2, G 264–012 and Gl 393 were catalogued before as potential targets for RV surveys for exoplanets. However, only Gl 393 was extensively monitored by HARPS (Bonfils et al. 2013), HIRES (Butler et al. 2017), and ESPRESSO (Hoggatpanah et al. 2019). In contrast, G 264–012 was not observed with high-precision RVs until now. The exoplanet Gl 393 b may have passed unnoticed due to its low mass and the strong impact

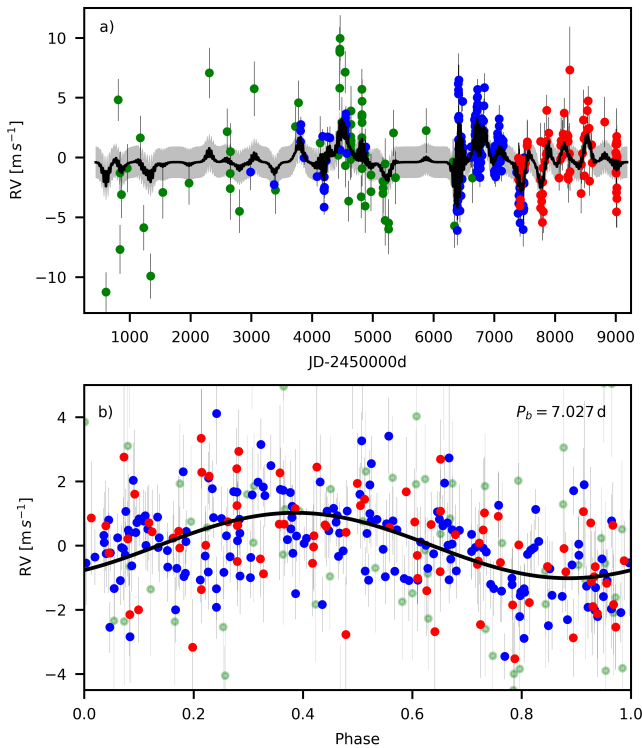


Fig. 14. Gl 393. *Panel a*): GP fit (black solid line) and 1-sigma uncertainties (grey area) to the RV data of HIRES (green points), HARPS (blue points) and CARMENES VIS channel (red squares). *Panel b*): activity subtracted RVs, phase-folded to the 7.03 d period. The Keplerian model (black solid line) is overplotted.

of the magnetic activity of the star on the RV variability. Fig. 15 shows that this planet produces the smallest RV semi-amplitude of any of all detected planets around M dwarfs.

In their catalogue of chromospheric activity and jitter measurements of 2630 stars in the California Planet Search with HIRES, Isaacson & Fischer (2010) found Gl 393 to be active and RV variable with a jitter of 3.174 m s^{-1} . Grandjean et al. (2020), using HARPS data, also found its RV curve to be dominated by spots. Though they used the correlation between RVs and the bisector velocity span (BVS; or the velocity span covered by the bisector of the cross-correlation function) to correct the RVs from the signal caused by spots, as in Melo et al. (2007), they still did not detect the planet.

At that time, the star showed an RV amplitude of 17.7 m s^{-1} (BVS of 24.5 m s^{-1}) and 1.2 and 3.6 m s^{-1} in the mean RV uncertainty and rms, respectively, whereas the CARMENES RV data acquired during the latter epochs has values of 1.5 and 2.3 m s^{-1} in the mean RV uncertainty and rms. The combined GP+Keplerian model takes a big leap in evidence, showing the much lower activity level of the star when the CARMENES data were obtained as compared with previous seasons. This is confirmed by the fact that the rotational period signal in our RVs loses power over the seasons.

The HARPS non-detection probably happened because their data were acquired during epochs when the star was dominated by activity. This shows that the detection of exoplanets depends on the activity level of the star which, in turn, depends on when the planet is observed within its activity cycle. Therefore, planets could be detected in moderately active M dwarfs if observed

Table 6. Gl 393: priors, best likelihood and average posterior parameter values of the planet plus activity fit to RVs, and derived planetary parameters.

| Parameter | Prior | Posterior | Unit |
|----------------------------------|--|---------------------------------|-------------------|
| <i>Planets</i> | | | |
| P_b | $\mathcal{U}(0, 100)$ | $7.02679^{+0.00082}_{-0.00085}$ | d |
| K_b | $\mathcal{U}(0, 5 \sigma_{\text{RV}})$ | $1.01^{+0.14}_{-0.14}$ | m s^{-1} |
| $t_{c,b} - 2458000$ | $\mathcal{U}(0, 100)$ | $2.72^{+0.21}_{-0.21}$ | d |
| <i>GP kernel hyperparameters</i> | | | |
| h | $\mathcal{U}(0, 5 \sigma_{\text{RV}})$ | $1.30^{+0.22}_{-0.21}$ | m s^{-1} |
| P | $\mathcal{U}(0, 220)$ | $35.0^{+7.6}_{-4.3}$ | d |
| λ | $\mathcal{U}(0, \sim 19000)$ | $54.3^{+13.6}_{-11.1}$ | d |
| w | $\mathcal{U}(0, 1)$ | $0.73^{+0.13}_{-0.13}$ | |
| <i>Instruments</i> | | | |
| σ_{HIRES} | $\mathcal{U}(0, 3 \sigma_{\text{RV}})$ | $1.927^{+0.406}_{-0.474}$ | m s^{-1} |
| μ_{HIRES} | $\mathcal{U}(\mu_1, \mu_2)$ | $-0.39^{+0.52}_{-0.52}$ | m s^{-1} |
| σ_{HARPS} | $\mathcal{U}(0, 3 \sigma_{\text{RV}})$ | $0.004^{+0.128}_{-0.071}$ | m s^{-1} |
| μ_{HARPS} | $\mathcal{U}(\mu_1, \mu_2)$ | $-4.25^{+0.41}_{-0.42}$ | m s^{-1} |
| $\sigma_{\text{C.VIS}}$ | $\mathcal{U}(0, 3 \sigma_{\text{RV}})$ | $0.015^{+0.246}_{-0.143}$ | m s^{-1} |
| $\mu_{\text{C.VIS}}$ | $\mathcal{U}(\mu_1, \mu_2)$ | $0.23^{+0.52}_{-0.52}$ | m s^{-1} |
| <i>Derived</i> | | | |
| a_b | | $0.05402^{+0.00072}_{-0.00072}$ | au |
| $M_b \sin i$ | | $1.71^{+0.24}_{-0.24}$ | M_{\oplus} |
| S_b | | $9.21^{+0.31}_{-0.31}$ | S_{\oplus} |
| $T_{\text{eq},b}$ | | 485^{+11}_{-11} | K |

during their magnetic cycle minima or, at least, away from their maxima, when activity signals dominate their time series.

5.2. The three planets in context

Being M4.0V and M2.0V spectral-type stars, G 264–012 and Gl 393 have liquid-water habitable zones with optimistic inner edges at 0.087 and 0.136 au from their stars, respectively (Kopparapu et al. 2013). The three planets in these two systems orbit closer to their stars, at 0.023 and 0.053 au, for planets G 264–012 b and c, and at 0.054 au for Gl 393 b, than these optimistic limits. At the distances from their stars given by their semi-major axes, all three planets receive larger fluxes than that received at Earth from the Sun, reaching higher equilibrium temperature, assuming zero Bond albedo (see Tables 5 and 6).

As can be seen in Fig. 15, all three planets lie on the Earth-mass region of the parameter space of the mass versus period diagram. The ratios of the minimum mass of the planets to that of the star for both systems is similar, with values of 6.32 and 1.21 times 10^{-5} for G 264–012 and Gl 393, respectively.

5.3. Formation scenarios

The three planets presented in this paper are close-in (super-)Earths and representations of the lower-mass end of their population. Previous findings of similar planets (e.g. Luque et al. 2019), as well as theoretical works (Burn et al., accepted), sug-

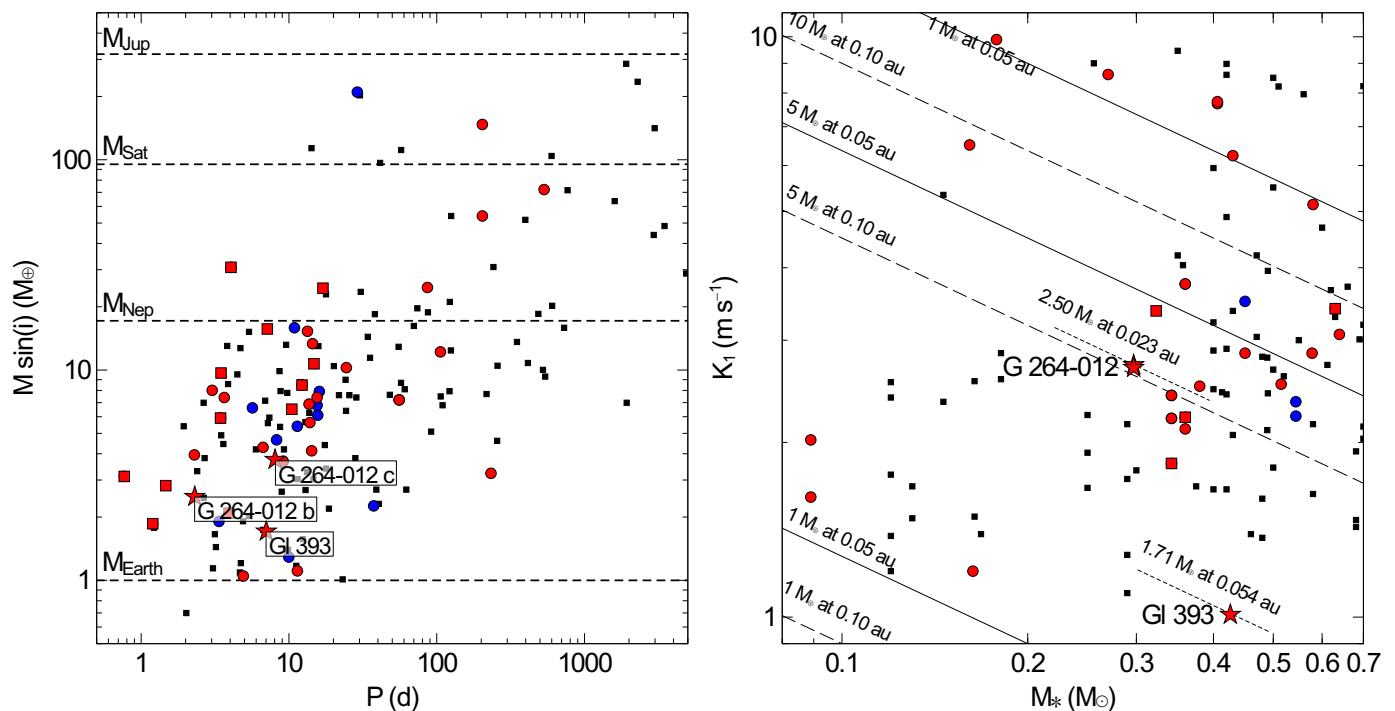


Fig. 15. Parameters of all known exoplanets around M dwarfs. *Left panel:* Minimum planet mass versus orbital period. *Right panel:* RV curve semi-amplitude against host stellar mass. Black squares represent exoplanet parameters for those listed in <http://exoplanets.eu> on 01 February 2021 and cyan small circles represent TESS detections. Red symbols show planets detected by the CARMENES survey (solid circles) or by its follow-up of TESS detections (solid squares). The three planet candidates presented in this work are shown as red stars.

gest that the planets we detected are a frequent outcome of planet formation around M dwarfs. The solar metallicities of the host stars are thought to be favourable for the formation of such inner low-mass planet systems (Schlecker et al. 2020).

Planets of this type are thought to form via core accretion (Perri & Cameron 1974; Mizuno et al. 1978; Mizuno 1980), which relies on the accretion of solid material via planetesimals and smaller particles. The accretion of these smaller particles, or ‘pebbles’, typically millimetre- to centimetre-sized bodies, was shown to be very efficient in growing planetary cores (Ormel & Klahr 2010; Lambrechts & Johansen 2012). Since fresh supply of such material is ensured by a radial flux in the protoplanetary disc (Lambrechts & Johansen 2014), there must be some mechanism at work that stops the accretion to ultimately yield the low masses that we measure. Plausible mechanisms for such a cut-off are self-isolation through perturbations of the surrounding disc (Morbidelli & Nesvorný 2012; Lambrechts et al. 2014) or the emergence of a hypothetical massive outer companion (e.g. Ormel 2017).

However, M-dwarf planets similar to G 264–012 b and c and Gl 393 b are also well reproduced by models that grow planetary cores only via accretion of planetesimals and do not take into account pebble accretion (e.g. Emsenhuber et al. 2020). This variant requires no assumptions about a pebble blocking mechanism.

Both models typically assume the formation of planets further out with a subsequent migration, but in-situ formation of super-Earths may be possible under certain conditions, such as super-solar metallicity of the host star (e.g. Schlaufman 2014). Our discovery reinforces the emerging paradigm that the formation of compact systems of low-mass planets around M dwarfs is the rule rather than the exception.

5.4. Planet detectability

Though the data at hand are insufficient to unequivocally distinguish between the different formation models, they provide constraints for the existence of larger outer planets in these two systems. To this aim, we estimated, for each of our two stars, the maximum $M \sin i$ value compatible with the RV measurements as a function of prospective orbital period. First, we verified that the RVs of our two stars did not show long-term trends, which would have needed correction, and fitted the data to a circular orbit using a partially-linearised, least-squares fitting procedure¹⁴ (James & Roos 1975) as a function of different orbital periods P . For each prospective P , we then determined the best-fit semi-amplitude $K(P)$ and computed a planet mass value $M \sin i_{\text{max}}(P) = M_m(P)$ using the mass of the star. This mass is the maximum a planet can have to be non-detectable in our RV time series, considering their respective noise characteristics.

Figure 16 shows $M_m(P)$ as a function of the orbital period for G 264–012 and Gl 393. Both stars have good quality observations, with a large number of data points. Nonetheless, the much longer baseline and larger number of RVs acquired for Gl 393, with three different instruments, make this data set sensitive to planets with masses as low as $M \sin i \approx 0.3 M_{\oplus}$ for $P < 3$ d and below $1.0 M_{\oplus}$ for periods up to 2000 d. The sensitivity of G 264–012 RV data set is somewhat less due to the shorter time span of its time series acquired with CARMENES only (compare dark-grey areas for both stars in Fig. 16). For this star, the change of slope of the sensitivity for periods beyond the length of the data set is apparent at around 1400 d. The figure also shows the differences in detectability of our raw data (no cleaning of plan-

¹⁴ Minuit: <https://iminuit.readthedocs.io/en/stable/about.html>

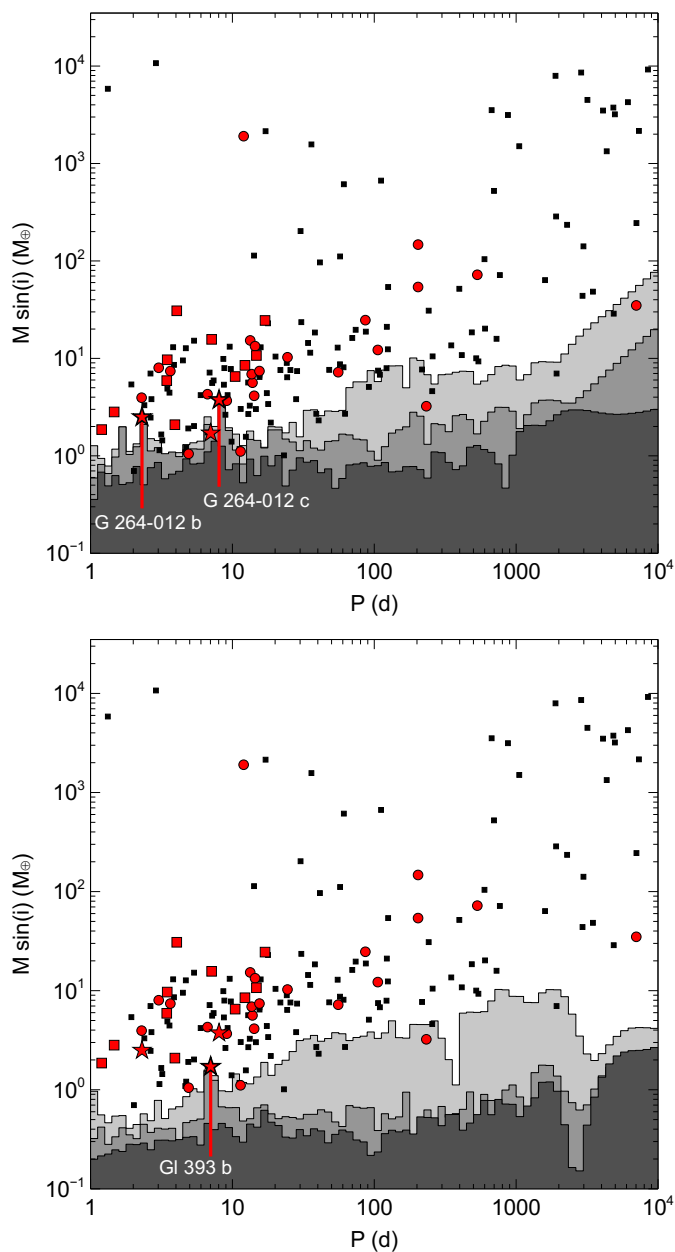


Fig. 16. Maximum $M \sin i$ value compatible with the RV measurements as a function of prospective orbital period. *Upper panel:* for G 264–012 RV curve. *Lower panel:* Gl 393 RV curve. From light to darker grey, detectability from original RV data (no modelling of planets or activity), data corrected for activity with GP, and data corrected from both, activity and planet signals. Symbols are the same as in Fig. 15 with the planets in each of the two systems labelled only with b, c for G 264–012 and b for Gl 393.

ets or activity) compared with data cleaned from activity using GP, and fully cleaned data from planetary and activity signals. By removing the activity, the peak corresponding to Gl 393 b becomes more significant in the detectability maps. After removing the RV variability produced by the activity and the planets, the remaining detectability functions show a higher sensitivity at all periods.

These RVs disprove the presence in the system of planets larger than $\sim 1.0 M_{\oplus}$ around G 264–012 up to periods of 1000 d. Gl 393 does not show signs of any other planet with mass above $\sim 0.5 M_{\oplus}$ up to periods of 100 d and up to $\sim 1.0 M_{\oplus}$ in the 100–

1000 d period range. In Fig. 16, we also plot all known exoplanets around M dwarfs, showing that our RVs are of enough quality to show the signal of any of those planets if they had been orbiting our systems.

5.5. Dynamical stability of G264-012

In this subsection, we seek to test the stability of the G264-012 system by varying the parameters that remained unconstrained after the global model: the inclination of the system from the observer point of view, which directly affects the real masses of the planets, and their eccentricities. We note that the natural trend of planetary systems is to reside in a nearly co-planar configuration; hence, we assumed planets b and c as being co-planar. This choice was further motivated by the results yielded by Kepler and the HARPS survey, which suggest that the mutual inclinations of multi-planet systems are of the order ≤ 10 deg (see e.g. Fabrycky et al. 2014).

To this end, we made use of the Mean Exponential Growth factor of Nearby Orbits (MEGNO) chaos index, $Y(t)$ (Cincotta & Simó 1999, 2000; Cincotta et al. 2003). MEGNO is extensively used to test the stability of many planetary systems (e.g. Jenkins et al. 2019; Pozuelos et al. 2020; Demory et al. 2020). In particular, its time-averaged mean value, $\langle Y(t) \rangle$, amplifies any stochastic behaviour, allowing for the detection of hyperbolic regions during the integration time. Hence, $\langle Y(t) \rangle$ allows us to distinguish between chaotic and stable trajectories: if $\langle Y(t) \rangle \rightarrow \infty$ for $t \rightarrow \infty$, the system is chaotic; while if $\langle Y(t) \rangle \rightarrow 2$ for $t \rightarrow \infty$, the motion is stable. We used the MEGNO implementation within the N-body integrator REBOUND (Rein & Liu 2012), which makes use of the Wisdom-Holman WHFast code (Rein & Tamayo 2015).

First, we evaluated the inclination of the system 1000 times, investigating values from 10 to 90 deg. Our choice to limit the inclination to 10 deg is twofold; first, randomly oriented systems disfavour small values of inclination (see e.g. Dreizler et al. 2020); and second, orbital inclinations close to zero (face on) disfavour the detection of planetary systems via RVs. From our global analysis, the results hint that planets b and c reside in circular orbits; hence, in this case we considered zero eccentricity for both planets. We found that the system tolerated the full range of inclinations explored with a $\Delta \langle Y(t) \rangle = 2.0 - \langle Y(t) \rangle < 10^{-3}$. This dynamical robustness impeded strong constraints on the system’s inclination, and consequently on the planetary masses. While our global model favoured circular orbits, mutual interactions between planets b and c may still produce orbital excitations which introduce some level of eccentricities. Then, to estimate their maximum values without disrupting the system’s stability, we conducted a second suite of simulations by allowing the planets to have eccentric orbits at different system’s inclinations. We built stability maps e_b – e_c for discrete sample of inclinations of 90, 70, 50, 30 and 10 deg, and eccentricities in the range 0.0–0.3. We took 10 values from this range, meaning that the size of each stability map was 10×10 pixels. We found that, in the case of maximum system inclination (90 deg), that is, minimum planet masses, both planets must have eccentricities < 0.3 to ensure the stability of the system. In the case of minimum inclination (10 deg), or when the masses of the planets are closer to their maximum values, the eccentricities must be < 0.1 . This means that, while circular orbits represent the most plausible architecture of the system with the data at hand, planets b and c may tolerate a certain level of eccentricity, but in all cases the eccentricity are very likely to be below 0.3. In all our simulations, the integration time was set to 10^6 times the orbital period

of the outermost planet, c, and the integration time-step was 5% the orbital period of the innermost one, b.

6. Conclusions

We studied two systems within the CARMENES survey of exoplanets around M dwarfs. Our analyses of CARMENES-only data for G 264–012 and of CARMENES, HARPS, and HIRES RV data for Gl 393 suggest that these two stars are orbited by two and one super-Earth planets, respectively. The planets around G 264–012 have minimum masses of 2.5 and 3.8 M_{\oplus} with orbital periods of 2.3 and 8.1 d, corresponding to semi-major axes of 0.02 and 0.05 au. We calculated the equilibrium temperature of G 264–012 b and c to be around 590 and 380 K, respectively. Gl 393 is orbited by a terrestrial planet with an orbital period of 7 d. Gl 393 b has a minimum mass of roughly 1.7 M_{\oplus} , and is orbiting its host star at a distance of approximately 0.054 au. Its equilibrium temperature is estimated to be of around 480 K.

Our minimum mass and temperature estimates put the planets into the family of hot Earths and Super-Earths. Since they receive total radiative fluxes larger than that of Earth, the planets are too close to the host star for the possible existence of liquid water on their surfaces.

The exoplanets in these two systems fulfil all the characteristics to be perfect targets for radio observations to test the star-planet interaction scenario. This hypothesis was recently put forward to explain the detection of coherent circularly polarised radio emission in GJ 1151 (Vedantham et al. 2020). This type of emission was even found to be modulated with the orbital period of the planet in the only other instance of such detections, Proxima Centauri (Pérez-Torres et al. 2021). For the two systems described in this work, the computed flux density expected from the star-planet interaction is within the reach of current radio interferometers.

The detection of auroral radio emission from the stars periodically modulated with the orbital period of the planet, as shown for Proxima b (Pérez-Torres et al. 2021), would be clear evidence of star-planet interaction. In the case of GJ 1151, a RV signal ascribed to a possible candidate planet at an orbital period suggested by the previously detected radio emission was found by Mahadevan et al. (2021) but later refuted by Perger et al. (2021b). The detection of such emission, with the required characteristics, in the two systems presented in this work would independently confirm the presence of their exoplanets and help validate radio observations as a completely new and independent planet-detection technique.

Acknowledgements. CARMENES is an instrument for the Centro Astronómico Hispano-Alemán (CAHA) at Calar Alto (Almería, Spain), operated jointly by the Junta de Andalucía and the Instituto de Astrofísica de Andalucía (CSIC). CARMENES was funded by the Max-Planck-Gesellschaft (MPG), the Consejo Superior de Investigaciones Científicas (CSIC), the Ministerio de Economía y Competitividad (MINECO) and the European Regional Development Fund (ERDF) through projects FICTS-2011-02, ICTS-2017-07-CAHA-4, and CAHA16-CE-3978, and the members of the CARMENES Consortium (Max-Planck-Institut für Astronomie, Instituto de Astrofísica de Andalucía, Landessternwarte Königstuhl, Institut de Ciències de l’Espai, Institut für Astrophysik Göttingen, Universidad Complutense de Madrid, Thüringer Landessternwarte Tautenburg, Instituto de Astrofísica de Canarias, Hamburger Sternwarte, Centro de Astrobiología and Centro Astronómico Hispano-Alemán), with additional contributions by the MINECO, the Deutsche Forschungsgemeinschaft through the Major Research Instrumentation Programme and Research Unit FOR2544 “Blue Planets around Red Stars”, the Klaus Tschira Stiftung, the states of Baden-Württemberg and Niedersachsen, and by the Junta de Andalucía. We acknowledge financial support from the Agencia Estatal de Investigación of the Ministerio de Ciencia, Innovación y Universidades and the ERDF through projects PID2019-109522GB-C51[1:4]/AEI/10.13039/501100011033, PGC2018-098153-B-C33, AYA2017-

89637-R and the Centre of Excellence “Severo Ochoa” and “María de Maeztu” awards to the Instituto de Astrofísica de Canarias (SEV-2015-0548), Instituto de Astrofísica de Andalucía (SEV-2017-0709), and Centro de Astrobiología (MDM-2017-0737), the Fundação para a Ciência e a Tecnologia and the ERDF (COMPETE2020), the Programa Operacional Competitividade e Internacionalização (UID/FIS/04434/2019, UIDB/04434/2020, UIDP/04434/2020, PTDC/FIS-AST/[32113,28953,28987]/2017 & POCI-01-0145-FEDER-[032113,028953,028987]), the Generalitat de Catalunya (CERCA programme), the European Research Council under the Horizon 2020 Framework programme (ERC Advanced Grant Origins 832428), FONDECYT (3180063), the Swiss National Science Foundation for supporting research with HARPS (SNSF 140649, 152721, 166227, and 184618), and NASA (NNX17AG24G). This publication made use of the SIMBAD database, the Aladin sky atlas, and the VizieR catalogue access tool developed at CDS, Strasbourg Observatory, France, the Python libraries Matplotlib, NumPy, and SciPy, the collection of software packages AstroPy and topfplotter, and data from the CARMENES data archive at CAB (CSIC-INTA), the ESO Science Archive Facility under request number vperdelw-552557, the TESS mission, obtained from the MAST data archive at the Space Telescope Science Institute (STScI), and the K2 mission.

References

- Aller, A., Lillo-Box, J., Jones, D., Miranda, L. F., & Barceló Forteza, S. 2020, *A&A*, 635, A128
- Alonso-Floriano, F. J., Morales, J. C., Caballero, J. A., et al. 2015, *A&A*, 577, A128
- Ambikasaran, S., Foreman-Mackey, D., Greengard, L., Hogg, D. W., & O’Neil, M. 2015, *IEEE Transactions on Pattern Analysis and Machine Intelligence*, 38, 252
- Andretta, V., Doyle, J. G., & Byrne, P. B. 1997, *A&A*, 322, 266
- Anglada-Escudé, G. & Butler, R. P. 2012, *ApJS*, 200, 15
- Angus, R., Morton, T., Aigrain, S., Foreman-Mackey, D., & Rajpaul, V. 2018, *MNRAS*, 474, 2094
- Argelander, F. W. A. 1859, *Bonner Sternverzeichnis*, 1.
- Astudillo-Defru, N., Delfosse, X., Bonfils, X., et al. 2017, *A&A*, 600, A13
- Baluev, R. V. 2013, *MNRAS*, 429, 2052
- Baroch, D., Morales, J. C., Ribas, I., et al. 2020, *A&A*, 641, A69
- Bauer, F. F., Zechmeister, M., Kaminski, A., et al. 2020, *A&A*, 640, A50
- Bauer, F. F., Zechmeister, M., & Reiners, A. 2015, *A&A*, 581, A117
- Berta, Z. K., Irwin, J., Charbonneau, D., Burke, C. J., & Falco, E. E. 2012, *AJ*, 144, 145
- Bianchi, L., Conti, A., & Shiao, B. 2014, *Advances in Space Research*, 53, 900
- Billier, B. A., Liu, M. C., Wahhaj, Z., et al. 2013, *ApJ*, 777, 160
- Bluhm, P., Luque, R., Espinoza, N., et al. 2020, *A&A*, 639, A132
- Bonfils, X., Delfosse, X., Udry, S., et al. 2013, *A&A*, 549, A109
- Boro Saikia, S., Marvin, C. J., Jeffers, S. V., et al. 2018, *A&A*, 616, A108
- Bower, G. C., Bolatto, A., Ford, E. B., & Kalas, P. 2009, *ApJ*, 701, 1922
- Brown, T. M., Baliber, N., Bianco, F. B., et al. 2013, *PASP*, 125, 1031
- Butler, R. P., Marcy, G. W., Williams, E., et al. 1996, *PASP*, 108, 500
- Butler, R. P., Vogt, S. S., Laughlin, G., et al. 2017, *AJ*, 153, 208
- Caballero, J. A., Guàrdia, J., López del Fresno, M., et al. 2016, in *Society of Photo-Optical Instrumentation Engineers (SPIE) Conference Series*, Vol. 9910, Proc. SPIE, 99100E
- Cifuentes, C., Caballero, J. A., Cortés-Contreras, M., et al. 2020, *A&A*, 642, A115
- Cincotta, P. & Simó, C. 1999, *Celestial Mechanics and Dynamical Astronomy*, 73, 195
- Cincotta, P. M., Giordano, C. M., & Simó, C. 2003, *Physica D Nonlinear Phenomena*, 182, 151
- Cincotta, P. M. & Simó, C. 2000, *A&AS*, 147, 205
- Cortés-Contreras, M. 2016, PhD thesis, Universidad Complutense de Madrid, Spain
- Dekker, H., D’Odorico, S., Kaufer, A., Delabre, B., & Kotzlowski, H. 2000, in *Society of Photo-Optical Instrumentation Engineers (SPIE) Conference Series*, Vol. 4008, Proc. SPIE, ed. M. Iye & A. F. Moorwood, 534–545
- Demory, B. O., Pozuelos, F. J., Gómez Maqueo Chew, Y., et al. 2020, *A&A*, 642, A49
- Díez Alonso, E., Caballero, J. A., Montes, D., et al. 2019, *A&A*, 621, A126
- Dittmann, J. A., Irwin, J. M., Charbonneau, D., & Berta-Thompson, Z. K. 2014, *ApJ*, 784, 156
- Dittmann, J. A., Irwin, J. M., Charbonneau, D., & Newton, E. R. 2016, *ApJ*, 818, 153
- Douglas, S. T., Curtis, J. L., Agüeros, M. A., et al. 2019, *ApJ*, 879, 100
- Dreizler, S., Jeffers, S. V., Rodríguez, E., et al. 2020, *MNRAS*, 493, 536
- Dressing, C. D. & Charbonneau, D. 2015, *ApJ*, 807, 45
- Eggen, O. J. 1958, *MNRAS*, 118, 65

- Eggen, O. J. 1991, *AJ*, 102, 2028
 Eggen, O. J. 1995, *AJ*, 110, 2862
 Eggen, O. J. 1998, *AJ*, 116, 284
 Emsenhuber, A., Mordasini, C., Burn, R., et al. 2020, arXiv e-prints, arXiv:2007.05561
 Espinoza, N., Kossakowski, D., & Brahm, R. 2019, *MNRAS*, 490, 2262
 Fabrycky, D. C., Lissauer, J. J., Ragozzine, D., et al. 2014, *ApJ*, 790, 146
 Findeisen, K., Hillenbrand, L., & Soderblom, D. 2011, *AJ*, 142, 23
 Fischer, D. A. & Marcy, G. W. 1992, *ApJ*, 396, 178
 Foreman-Mackey, D., Agol, E., Angus, R., & Ambikasaran, S. 2017, *AJ*, 154, 220
 Foreman-Mackey, D., Hogg, D. W., Lang, D., & Goodman, J. 2013, *PASP*, 125, 306
 Frith, J., Pinfield, D. J., Jones, H. R. A., et al. 2013, *MNRAS*, 435, 2161
 Fuhrmeister, B., Czesla, S., Schmitt, J. H. M. M., et al. 2019, *A&A*, 623, A24
 Gagné, J., Mamajek, E. E., Malo, L., et al. 2018, *ApJ*, 856, 23
 Gaia Collaboration. 2020, *VizieR Online Data Catalog*, I/350
 Gaia Collaboration, Brown, A. G. A., Vallenari, A., et al. 2018, *A&A*, 616, A1
 Gaidos, E., Mann, A. W., Lépine, S., et al. 2014, *MNRAS*, 443, 2561
 Giclas, H. L., Burnham, R., & Thomas, N. G. 1971, Lowell proper motion survey Northern Hemisphere. The G numbered stars. 8991 stars fainter than magnitude 8 with motions $> 0''.26$ /year
 Gilbertson, C., Ford, E. B., Jones, D. E., & Stenning, D. C. 2020, *ApJ*, 905, 155
 Gliese, W. 1969, *Veröffentlichungen des Astronomischen Rechen-Instituts Heidelberg*, 22, 1
 González-Álvarez, E. 2014, Master's thesis, Universidad Complutense de Madrid, Spain
 Grandjean, A., Lagrange, A. M., Keppler, M., et al. 2020, *A&A*, 633, A44
 Hardegree-Ullman, K. K., Cushing, M. C., Muirhead, P. S., & Christiansen, J. L. 2019, *AJ*, 158, 75
 Harp, G. R., Richards, J., Tarter, J. C., et al. 2016, *AJ*, 152, 181
 Haywood, R. D., Collier Cameron, A., Queloz, D., et al. 2014, *MNRAS*, 443, 2517
 Hippke, M. & Heller, R. 2019, *A&A*, 623, A39
 Hojjatpanah, S., Figueira, P., Santos, N. C., et al. 2019, *A&A*, 629, A161
 Howell, S. B., Soberg, C., Haas, M., et al. 2014, *PASP*, 126, 398
 Husser, T. O., Wende-von Berg, S., Dreizler, S., et al. 2013, *A&A*, 553, A6
 Isaacson, H. & Fischer, D. 2010, *ApJ*, 725, 875
 James, F. & Roos, M. 1975, *Computer Physics Communications*, 10, 343
 Janson, M., Bergfors, C., Brandner, W., et al. 2014, *ApJ*, 789, 102
 Jeffers, S. V., Dreizler, S., Barnes, J. R., et al. 2020, *Science*, 368, 1477
 Jeffers, S. V., Schöfer, P., Lamert, A., et al. 2018, *A&A*, 614, A76
 Jenkins, J. S., Pozuelos, F. J., Tuomi, M., et al. 2019, *MNRAS*, 490, 5585
 Kaufer, A., Stahl, O., Tubbesing, S., et al. 1999, *The Messenger*, 95, 8
 Kochanek, C. S., Shappee, B. J., Stanek, K. Z., et al. 2017, *PASP*, 129, 104502
 Koppappu, R. K., Ramirez, R., Kasting, J. F., et al. 2013, *ApJ*, 765, 131
 Lafarga, M., Ribas, I., Lovis, C., et al. 2020, *A&A*, 636, A36
 Lafrenière, D., Doyon, R., Marois, C., et al. 2007, *ApJ*, 670, 1367
 Lambrechts, M. & Johansen, A. 2012, *A&A*, 544, A32
 Lambrechts, M. & Johansen, A. 2014, *A&A*, 572, A107
 Lambrechts, M., Johansen, A., & Morbidelli, A. 2014, *A&A*, 572, A35
 Landolt, A. U. 1983, *AJ*, 88, 439
 Leggett, S. K. 1992, *ApJS*, 82, 351
 Lenz, P. & Breger, M. 2005, *Communications in Asteroseismology*, 146, 53
 Lépine, S. & Gaidos, E. 2011, *AJ*, 142, 138
 Lépine, S., Hilton, E. J., Mann, A. W., et al. 2013, *AJ*, 145, 102
 Lépine, S. & Shara, M. M. 2005, *AJ*, 129, 1483
 López-Morales, M., Haywood, R. D., Coughlin, J. L., et al. 2016, *AJ*, 152, 204
 López-Santiago, J., Micela, G., & Montes, D. 2009, *A&A*, 499, 129
 López-Santiago, J., Montes, D., Crespo-Chacón, I., & Fernández-Figueroa, M. J. 2006, *ApJ*, 643, 1160
 Luhman, K. L., Stauffer, J. R., & Mamajek, E. E. 2005, *ApJ*, 628, L69
 Luque, R., Pallé, E., Kossakowski, D., et al. 2019, *A&A*, 628, A39
 Luyten, W. J. 1979, *New Luyten Catalogue of stars with proper motions larger than two tenths of an arcsecond*
 Mahadevan, S., Stefánsson, G., Robertson, P., et al. 2021, arXiv e-prints, arXiv:2102.02233
 Malo, L., Doyon, R., Lafrenière, D., et al. 2013, *ApJ*, 762, 88
 Martin, D. C., Fanson, J., Schiminovich, D., et al. 2005, *ApJ*, 619, L1
 Martin, J., Fuhrmeister, B., Mittag, M., et al. 2017, *A&A*, 605, A113
 Masciadri, E., Mundt, R., Henning, T., Alvarez, C., & Barrado y Navascués, D. 2005, *ApJ*, 625, 1004
 Mayor, M., Pepe, F., Queloz, D., et al. 2003, *The Messenger*, 114, 20
 Melo, C., Santos, N. C., Gieren, W., et al. 2007, *A&A*, 467, 721
 Mizuno, H. 1980, *Progress of Theoretical Physics*, 64, 544
 Mizuno, H., Nakazawa, K., & Hayashi, C. 1978, *Progress of Theoretical Physics*, 60, 699
 Montes, D., López-Santiago, J., Fernández-Figueroa, M. J., & Gálvez, M. C. 2001, *A&A*, 379, 976
 Morales, J. C., Mustill, A. J., Ribas, I., et al. 2019, *Science*, 365, 1441
 Morbidelli, A. & Nesvorný, D. 2012, *A&A*, 546, A18
 Naud, M.-E., Artigau, É., Doyon, R., et al. 2017, *AJ*, 154, 129
 Nava, C., López-Morales, M., Haywood, R. D., & Giles, H. A. C. 2020, *AJ*, 159, 23
 Newton, E. R., Irwin, J., Charbonneau, D., et al. 2016, *ApJ*, 821, 93
 Nielsen, E. L. & Close, L. M. 2010, *ApJ*, 717, 878
 Ormel, C. W. 2017, *The Emerging Paradigm of Pebble Accretion*, ed. M. Pessah & O. Gressel, Vol. 445, 197
 Ormel, C. W. & Klahr, H. H. 2010, *A&A*, 520, A43
 Passegger, V. M., Reiners, A., Jeffers, S. V., et al. 2018, *A&A*, 615, A6
 Passegger, V. M., Schweitzer, A., Shulyak, D., et al. 2019, *A&A*, 627, A161
 Pérez-Torres, M., Gómez, J. F., Ortiz, J. L., et al. 2021, *A&A*, 645, A77
 Perger, M., Anglada-Escudé, G., Ribas, I., et al. 2021a, *A&A*, 645, A58
 Perger, M., Ribas, I., Anglada-Escudé, G., et al. 2021b, arXiv e-prints, arXiv:2103.10216
 Perger, M., Scandariato, G., Ribas, I., et al. 2019, *A&A*, 624, A123
 Perri, F. & Cameron, A. G. W. 1974, *Icarus*, 22, 416
 Pojmanski, G. 1997, *Acta Astron.*, 47, 467
 Pollacco, D. L., Skillen, I., Collier Cameron, A., et al. 2006, *PASP*, 118, 1407
 Pozuelos, F. J., Suárez, J. C., de Elía, G. C., et al. 2020, *A&A*, 641, A23
 Quirrenbach, A., Amado, P. J., Caballero, J. A., et al. 2014, in *Society of Photo-Optical Instrumentation Engineers (SPIE) Conference Series*, Vol. 9147, Proc. SPIE, 91471F
 Quirrenbach, A., Amado, P. J., Ribas, I., et al. 2018, in *Society of Photo-Optical Instrumentation Engineers (SPIE) Conference Series*, Vol. 10702, Proc. SPIE, 107020W
 Rajpaul, V., Aigrain, S., Osborne, M. A., Reece, S., & Roberts, S. 2015, *MNRAS*, 452, 2269
 Rajpurohit, A. S., Allard, F., Rajpurohit, S., et al. 2018, *A&A*, 620, A180
 Rasmussen, C. E. & Williams, C. K. I. 2006, *Gaussian Processes for Machine Learning*
 Rebull, L. M., Stauffer, J. R., Hillenbrand, L. A., et al. 2017, *ApJ*, 839, 92
 Reid, I. N., Hawley, S. L., & Gizis, J. E. 1995, *AJ*, 110, 1838
 Rein, H. & Liu, S. F. 2012, *A&A*, 537, A128
 Rein, H. & Tamayo, D. 2015, *MNRAS*, 452, 376
 Reiners, A., Zechmeister, M., Caballero, J. A., et al. 2018, *A&A*, 612, A49
 Reinhold, T. & Hekker, S. 2020, *A&A*, 635, A43
 Ricker, G. R., Winn, J. N., Vanderspek, R., et al. 2015, *JATIS*, 1, 014003
 Ross, F. E. 1926, *AJ*, 37, 53
 Schäfer, S., Guenther, E. W., Reiners, A., et al. 2018, in *Society of Photo-Optical Instrumentation Engineers (SPIE) Conference Series*, Vol. 10702, Proc. SPIE, 1070276
 Schlaufman, K. C. 2014, *ApJ*, 790, 91
 Schlecker, M., Mordasini, C., Emsenhuber, A., et al. 2020, arXiv e-prints, arXiv:2007.05563
 Schneider, A. C., Greco, J., Cushing, M. C., et al. 2016, *ApJ*, 817, 112
 Schöfer, P., Jeffers, S. V., Reiners, A., et al. 2019, *A&A*, 623, A44
 Schweitzer, A., Passegger, V. M., Cifuentes, C., et al. 2019, *A&A*, 625, A68
 Skrutskie, M. F., Cutri, R. M., Stiening, R., et al. 2006, *AJ*, 131, 1163
 Stelzer, B., Marino, A., Micela, G., López-Santiago, J., & Liefke, C. 2013, *MNRAS*, 431, 2063
 Suárez Mascareño, A., Faria, J. P., Figueira, P., et al. 2020, *A&A*, 639, A77
 Suárez Mascareño, A., Reboló, R., & González Hernández, J. I. 2016, *A&A*, 595, A12
 Tal-Or, L., Trifonov, T., Zucker, S., Mazeh, T., & Zechmeister, M. 2019, *MNRAS*, 484, L8
 Tamuz, O., Mazeh, T., & Zucker, S. 2005, *MNRAS*, 356, 1466
 Terrien, R. C., Mahadevan, S., Deshpande, R., & Bender, C. F. 2015, *ApJS*, 220, 16
 Toledo-Padrón, B., Suárez Mascareño, A., González Hernández, J. I., et al. 2021, *A&A*, 648, A20
 Trifonov, T., Caballero, J. A., Morales, J. C., et al. 2021, *Science*, in press
 Trifonov, T., Kürster, M., Zechmeister, M., et al. 2018, *A&A*, 609, A117
 Trifonov, T., Tal-Or, L., Zechmeister, M., et al. 2020, *A&A*, 636, A74
 Tuomi, M., Jones, H. R. A., Barnes, J. R., Anglada-Escudé, G., & Jenkins, J. S. 2014, *MNRAS*, 441, 1545
 Vedantham, H. K., Callingham, J. R., Shimwell, T. W., et al. 2020, *Nature Astronomy*, 4, 577
 Vernet, J., Dekker, H., D'Odorico, S., et al. 2011, *A&A*, 536, A105
 Voges, W., Aschenbach, B., Boller, T., et al. 1999, *A&A*, 349, 389
 Vogt, S. S., Allen, S. L., Bigelow, B. C., et al. 1994, in *Society of Photo-Optical Instrumentation Engineers (SPIE) Conference Series*, Vol. 2198, Proc. SPIE, ed. D. L. Crawford & E. R. Craine, 362
 Wilson, R. E. 1953, *Carnegie Institute Washington D.C. Publication*, 0
 Zechmeister, M., Anglada-Escudé, G., & Reiners, A. 2014, *A&A*, 561, A59
 Zechmeister, M. & Kürster, M. 2009, *A&A*, 496, 577
 Zechmeister, M., Reiners, A., Amado, P. J., et al. 2018, *A&A*, 609, A12
 Zeng, L., Jacobsen, S. B., Sasselov, D. D., et al. 2019, *Proceedings of the National Academy of Science*, 116, 9723
 Zeng, L., Sasselov, D. D., & Jacobsen, S. B. 2016, *ApJ*, 819, 127

Zuckerman, B., Rhee, J. H., Song, I., & Bessell, M. S. 2011, *ApJ*, 732, 61

-
- ¹ Instituto de Astrofísica de Andalucía (IAA-CSIC), Glorieta de la Astronomía s/n, 18008 Granada, Spain e-mail: pja@iaa.csic.es
 - ² Instituto de Astrofísica de Canarias, Vía Láctea s/n, 38205 La Laguna, Tenerife, Spain
 - ³ Departamento de Astrofísica, Universidad de La Laguna, 38026 La Laguna, Tenerife, Spain
 - ⁴ Centro de Astrobiología (CSIC-INTA), ESAC, camino bajo del castillo s/n, 28049 Villanueva de la Cañada, Madrid, Spain
 - ⁵ Departamento de Física Teórica y del Cosmos, Universidad de Granada, 18071 Granada, Spain
 - ⁶ Institut de Ciències de l'Espai (ICE, CSIC), Campus UAB, c/de Can Magrans s/n, 08193 Bellaterra, Barcelona, Spain
 - ⁷ Institut d'Estudis Espacials de Catalunya (IEEC), C/Gran Capità 2-4, 08034 Barcelona, Spain
 - ⁸ Astrobiology Research Unit, University of Liège, Allée du 6 août, 19, 4000 Liège (Sart-Tilman), Belgium
 - ⁹ Max-Planck-Institut für Astronomie, Königstuhl 17, 69117 Heidelberg, Germany
 - ¹⁰ Landessternwarte, Zentrum für Astronomie der Universität Heidelberg, Königstuhl 12, 69117 Heidelberg, Germany
 - ¹¹ Institut für Astrophysik, Georg-August-Universität, Friedrich-Hund-Platz 1, 37077 Göttingen, Germany
 - ¹² Université de Grenoble Alpes, CNRS, IPAG, 38000 Grenoble, France
 - ¹³ Departamento de Matemática y Física Aplicadas, Universidad Católica de la Santísima Concepción, Alonso de Rivera 2850, Concepción, Chile
 - ¹⁴ Centro Astronómico Hispano-Alemán (CSIC-Junta de Andalucía), Observatorio Astronómico de Calar Alto, Sierra de los Filabres, 04550 Gérgal, Almería, Spain
 - ¹⁵ Astronomical Observatory of the University of Geneva, 51 ch. Pegasi, CH-1290 Versoix, Switzerland
 - ¹⁶ Thüringer Landessternwarte Tautenburg, Sternwarte 5, 07778 Tautenburg, Germany
 - ¹⁷ Facultad de Ciencias Físicas, Departamento de Física de la Tierra y Astrofísica & IPARCOS-UCM (Instituto de Física de Partículas y del Cosmos de la UCM), Universidad Complutense de Madrid, 28040 Madrid, Spain
 - ¹⁸ Department of Physics, Ariel University, Ariel 40700, Israel
 - ¹⁹ Department of Physics, University of Warwick, Gibbet Hill Road, Coventry CV4 7AL, UK
 - ²⁰ Instituto de Astrofísica e Ciências do Espaço, Universidade do Porto, CAUP, Rua das Estrelas, PT4150-762 Porto, Portugal
 - ²¹ Hamburger Sternwarte, Gojenbergsweg 112, 21029 Hamburg, Germany
 - ²² Departamento de Física e Astronomia, Faculdade de Ciências, Universidade do Porto, Rua do Campo Alegre, 4169-007 Porto, Portugal
 - ²³ Centro de Astrobiología (CSIC-INTA), Carretera de Ajalvir km 4, E-28850 Torrejón de Ardoz, Madrid, Spain
 - ²⁴ Max Planck Institute for Solar System Research, Justus-von-Liebigweg 3, 37077 Göttingen, Germany
 - ²⁵ Space sciences, Technologies and Astrophysics Research (STAR) Institute, Université de Liège, 19C Allée du 6 Août, B-4000 Liège, Belgium

Appendix A: Corner plot of MCMC posterior distributions

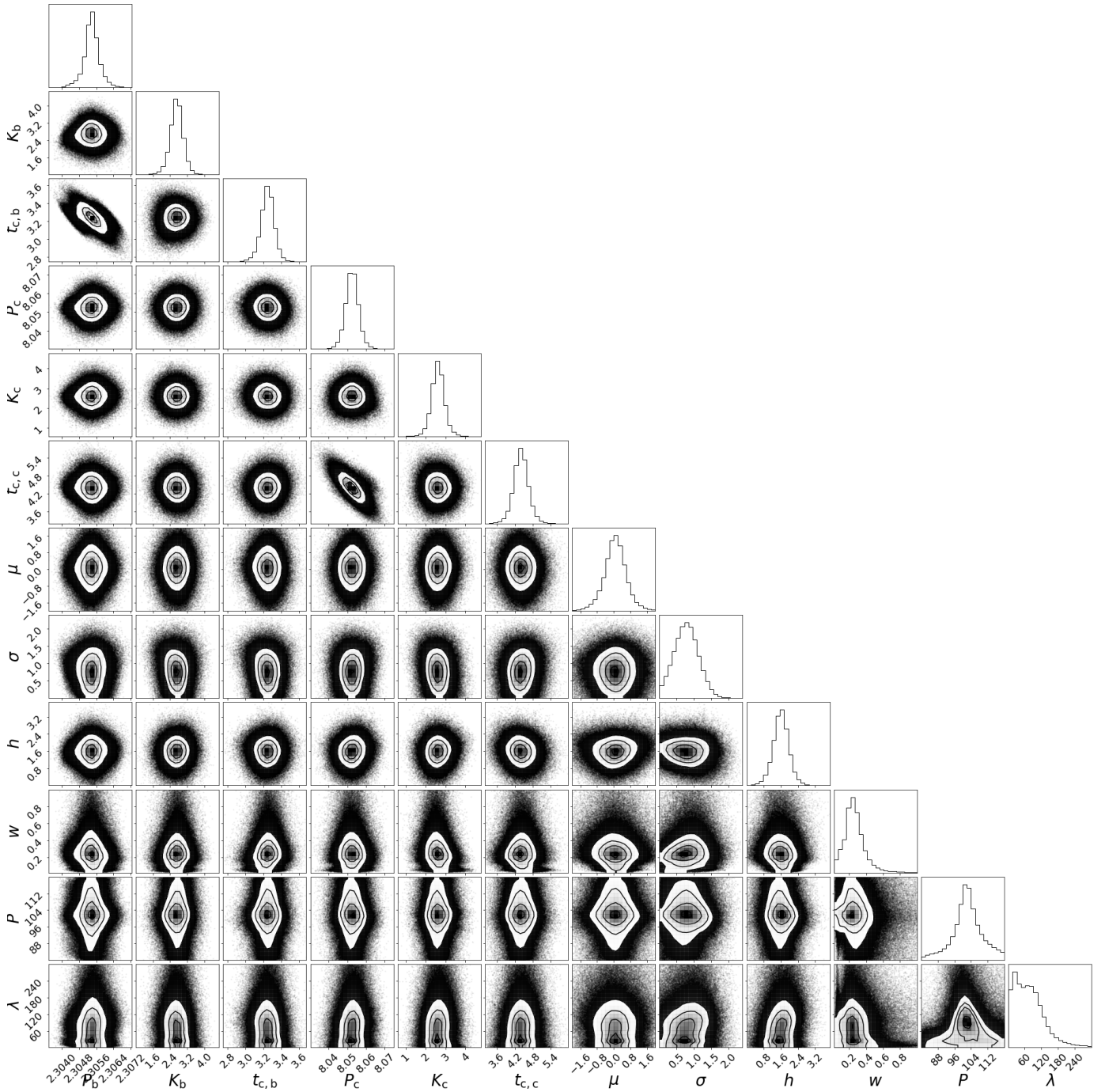


Fig. A.1. MCMC posterior distribution of the CARMENES VIS RVs for G264-012 for a model including two circular planetary orbits (parameters K_b , P_b , $T_{c,b}$, K_c , P_c , and $T_{c,c}$), a Gaussian Process using the `george`-code and a quasi-periodic kernel (hyper-parameters h , w , P , and λ), offset μ and additional jitter σ . Only solutions with $\ln \mathcal{L} > -410$ are shown.

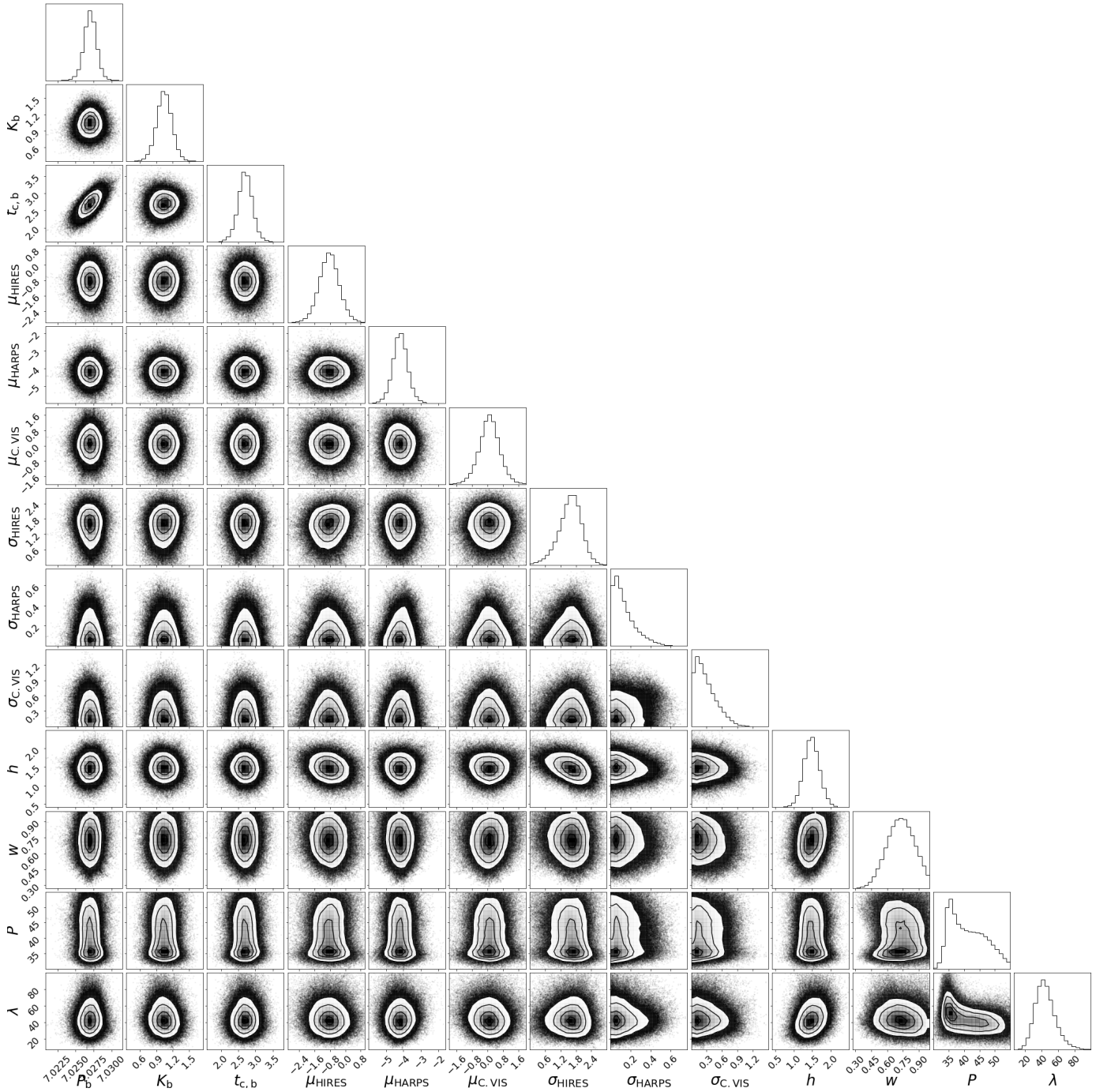


Fig. A.2. MCMC posterior distribution of the HIRES, HARPS, and CARMENES VIS RVs for G1393 for a model including one circular planetary orbit (parameters K_b , P_b , and $T_{c,b}$), a Gaussian Process using the george-code and a quasi-periodic kernel (hyper-parameters h , w , P , and λ), offsets (μ_{HIRES} , μ_{HARPS} , and $\mu_{\text{C.VIS}}$), and additional jitters (σ_{HIRES} , σ_{HARPS} , and $\sigma_{\text{C.VIS}}$). Only solutions with $\ln \mathcal{L} > -716$ are shown.

Appendix B: RV data**Table B.1.** Radial velocities of G264-012.^a

| BJD | RV [m s ⁻¹] | σ_{RV} [m s ⁻¹] | Instrument |
|---------------|-------------------------|------------------------------------|------------|
| 2457559.62513 | -1.20 | 1.20 | CARM-VIS |
| 2457597.54554 | -1.01 | 1.40 | CARM-VIS |
| 2457607.52688 | -7.97 | 1.72 | CARM-VIS |
| 2457613.49483 | -4.27 | 1.68 | CARM-VIS |
| 2457614.47815 | -6.42 | 1.48 | CARM-VIS |
| 2457618.51114 | 0.47 | 1.61 | CARM-VIS |
| 2457619.51990 | -6.91 | 1.55 | CARM-VIS |
| 2457621.49704 | -11.12 | 1.55 | CARM-VIS |
| 2457622.37542 | -5.41 | 1.51 | CARM-VIS |
| 2457625.46228 | 0.79 | 1.40 | CARM-VIS |
| ... | ... | ... | ... |

Notes. ^aThe full table is provided at CDS. We show here the first ten rows as a guidance.

Table B.2. Radial velocities of Gl 393.^a

| BJD | RV [m s ⁻¹] | σ_{RV} [m s ⁻¹] | Instrument |
|---------------|-------------------------|------------------------------------|------------|
| 2450607.77613 | -11.63 | 1.65 | HIRES |
| 2450807.12895 | 4.43 | 1.76 | HIRES |
| 2450837.91365 | -8.07 | 2.04 | HIRES |
| 2450839.02573 | -1.67 | 1.74 | HIRES |
| 2450861.94499 | -3.49 | 1.96 | HIRES |
| 2450955.86970 | -1.28 | 2.02 | HIRES |
| 2451172.05304 | 1.26 | 1.84 | HIRES |
| 2451227.97882 | -6.25 | 1.90 | HIRES |
| 2451342.79714 | -10.30 | 1.89 | HIRES |
| 2451544.16493 | -3.30 | 2.20 | HIRES |
| ... | ... | ... | ... |

Notes. ^a The full table is provided at CDS. We show here the first ten rows as a guidance.